Unrestrained ESCRT-III drives chromosome fragmentation and micronuclear catastrophe

Marina Vietri [1,2], Sebastian W. Schultz [1,2], Aurélie Bellanger [3], Carl M. Jones [4,5], Louise I. Petersen [3], Camilla Raiborg [1,2], Ellen Skarpen [1,2], Christeen Ramane J. Pedurupillay [6], Eline Kip [1,2], Romy Timmer [3], Ashish Jain [1,2], Philippe Collas [3], Roland L. Knorr [7,8], Sushma N. Grellscheid [4,5], Halim Kusumaatmaja [9], Andreas Brech [1,2], Francesca Micci [6], Harald Stenmark [1,2,*], and Coen Campsteijn [3,*]

[1] Centre for Cancer Cell Reprogramming, Faculty of Medicine, University of Oslo, Oslo, Norway

[2] Department of Molecular Cell Biology, Institute for Cancer Research, Oslo University Hospital, Oslo, Norway

[3] Department of Molecular Medicine, Institute of Basic Medicine, University of Oslo, Oslo, Norway

[4] Department of Biological Sciences, Durham University, Durham, UK

[5] Computational Biology Unit, Department of Biological Sciences, University of Bergen, Bergen, Norway

[6] Section for Cancer Cytogenetics, Institute for Cancer Genetics and Informatics, Oslo University Hospital, Oslo, Norway

[7] Max Plank Institute of Colloids and Interfaces, Department of Theory & Bio-Systems, Potsdam, Germany

[8] Dept. Biochemistry and Molecular Biology, Graduate School and Faculty of Medicine, University of Tokyo, Tokyo, Japan

[9] Department of Physics, Durham University, Durham, UK

[*] Corresponding authors: stenmark@ulrik.uio.no or coen.campsteijn@medisin.uio.no

Running title: ESCRT-mediated micronuclear catastrophe

Abstract

The ESCRT-III membrane fission machinery maintains nuclear envelope integrity. Whereas primary nuclei resealing takes minutes, micronuclear envelope ruptures appear to be irreversible. Micronuclear rupture result in catastrophic membrane collapse and is associated with chromosome fragmentation and chromothripsis, complex chromosome rearrangements thought to be a major driving force in cancer development. Here we use a combination of live microscopy and electron tomography to uncover the mechanisms that underlie micronuclear collapse after envelope rupture. We show that micronuclei inherently lack the capacity of primary nuclei to restrict accumulation of CHMP7-LEMD2, a compartmentalization sensor that detects loss of envelope integrity. This results in unrestrained ESCRT-III accumulation that drives extensive membrane deformation and DNA damage. Thus, the nuclear integrity surveillance machinery is a double-edged sword, as its sensitivity ensures rapid repair at primary nuclei while causing unrestrained activity at micronuclei, with catastrophic consequences for genome stability.

The endosomal sorting complex required for transport (ESCRT)-III forms filaments that drive membrane sealing essential to ensure integrity of the nuclear envelope. Competent ESCRT-III function is highly sensitive to balanced levels of the upstream factors that drive filament nucleation, and downstream effectors that control polymerization rates of these filaments, like the AAA^+ ATPase VPS4 [1-3]. To manipulate ESCRT-III function at the nuclear envelope, we established RPE1 cell lines allowing inducible expression of CHMP7, the most upstream component driving ESCRT-III processes at the nuclear envelope [4-6]. Whereas brief induction of CHMP7 expression was sufficient to induce CHMP4B accumulation, these CHMP4B foci were exclusively cytoplasmic (Fig. 1a top panel). This was consistent with reported localization for CHMP7 to the cytoplasm and endoplasmic reticulum (ER) [5,7], and suggested that subcellular localization of CHMP7 could be a key determinant to target CHMP4B foci to the nuclear envelope. We found that the CHMP7 C-terminal motif previously annotated as a MIM1 motif [2,8] represented a type 1a high-affinity nuclear export signal (NES) [9] (Extended Data Fig. 1a-c), providing a mechanism to actively exclude this 45kDa protein from the nucleus [10]. Inducible expression of a CHMP7 allele with a mutated NES ($CHMP7^{NES*}$) was sufficient to drive formation of persistent CHMP4B foci associated with the nuclear envelope as opposed to the ER (Fig. 1a, Extended Data Fig. 1d-i). Similar results were obtained when inducing wild type CHMP7 in the presence of

leptomycin B (LMB) to inhibit active nuclear export by Exportin 1 (XPO1), or upon fusion with 2 nuclear localization sequences (CHMP7^{NLS}) (Fig. 1a lower panels), arguing against an effect due to functional perturbation of the putative MIM1. This shows that nuclear entry of CHMP7 is key to its ability to induce CHMP4B filaments at the nuclear envelope.

The fact that CHMP7 accumulated in the nucleus upon abrogation of its active export (Fig. 1a) pointed towards active retention upon its diffusion into the nucleus. Indeed, nuclear CHMP7 retention and formation of CHMP4B foci was dependent on the presence of the inner nuclear membrane proteins LEMD2 and LEMD3 (Fig. 1b), in line with previous observations in yeast and during mammalian cell division [6,11]. In further support of this, in stable LEMD2-SNAPtag [12] CHMP4B-eGFP cells, nuclear retention of endogenous CHMP7 by LMB treatment specifically and reversibly induced the formation of CHMP4B foci at local LEMD2 enrichments (Fig. 1c and Extended Data Fig. 2, Movie 1).

In contrast to CHMP7, transient overexpression of LEMD2 or LEMD3 did not induce CHMP4B foci, but rather resulted in the rapid degradation of nucleoplasmic CHMP4B (Fig. 1d, Extended Data Fig. 3a-e, Movie 2). This phenotype depended on its C-terminal MSC (MAN1-Src1p C-terminal) domain (Extended Data Fig. 3c,d,f), previously reported to mediate interaction with CHMP7 [6]. Strikingly, co-expression of LEMD2 with nuclear CHMP7 (CHMP7^{NES*}) suppressed CHMP4B degradation and instead resulted in the formation of stable nuclear envelope foci highly enriched for CHMP4B, CHMP7^{NES*}, and LEMD2 (Fig. 1d, Extended Data Fig. 2c). These data show that XPO1-mediated export prevents untimely nuclear localization of CHMP7 and argue that nuclear influx of CHMP7 critically controls the formation of stable LEMD2-CHMP7 complexes that license CHMP4B polymerization.

We exploited the subcellular mislocalization of CHMP7^{NES*} to monitor effects of excessive nuclear CHMP7 and found that the CHMP4B foci corresponded to areas where the nuclear envelope underwent architectural deformations, as indicated by enrichment of the ER lumen marker mCherry-KDEL (Fig. 1e) and the inner nuclear membrane marker Lap2β (Extended Data Fig. 4a left panel). Furthermore, the absence of the nucleoporin Nup58 (Extended Data Fig. 4a right panel) and correlative light and electron microscope (CLEM) analysis (Fig. 1f) indicated that these foci do not represent aggregates of aberrant nuclear pore complexes [11,13]. CLEM analysis

revealed these membrane distortions to be complex 3-dimensional trabecular networks with tubular features (Fig. 1f). Consistent with their localization, CHMP7 resulted in remodelling of the ER without much effect on the nuclear envelope, CHMP7^{NLS} selectively distorted the inner nuclear membrane, and CHMP7^{NES*} affected both faces of the nuclear envelope (Fig. 1f, Extended Data Fig. 4b). Considering the dramatic membrane deformation [14-16], we assessed nuclear envelope integrity upon expression of these CHMP7 alleles by monitoring an mRuby3-NES fusion that requires nucleocytoplasmic compartmentalization for its exclusion from the nucleus. Whereas overexpression of LEMD2 or CHMP7 did not compromise nuclear integrity, cells expressing CHMP7^{NES*} or CHMP7^{NLS} underwent decompartmentalization within hours (Fig. 1g, Extended Data Fig. 4c-e), in a fashion dependent on the CHMP7 membrane-binding N-terminus [5] (Fig. 1g, Extended Data Fig. 4f) and the presence of LEMD2 and LEMD3 (Extended Data Fig. 4g). This was not due to defective mitotic nuclear envelope reformation as it was readily observed in cells that did not traverse mitosis (Movie 3). Taken together, our data show that nuclear entry of CHMP7, in addition to its association with LEMD2/LEMD3 and the nuclear envelope are the key prerequisites to trigger polymerization of CHMP4B [4,15,17,18]. Excessive nuclear influx of CHMP7 is sufficient to drive the formation of persistent ESCRT-III foci that instead deform the nuclear envelope to the point of irreversible loss of compartmentalization.

Missegregating chromosomes contained within micronuclei have been shown to be a source of massive chromosome rearrangements, chromothripsis, as well as pro-inflammatory signalling upon micronuclear membrane rupture [19-22]. Work over the last years has highlighted that defects in distribution of inner nuclear membrane components predisposes micronuclei to rupture [14,23,24], but the equally important question why micronuclei are not repaired has remained unaddressed. In line with previous observations [25,26], we observed that a significant fraction of micronuclei was enriched for endogenous CHMP4B and downstream ESCRT-III components in a range of cell lines (Extended Data Fig. 5a,b). To dissect the chain of events at micronuclei upon spontaneous rupture, we monitored CHMP4B dynamics at monopolar spindle 1 (MPS1)-inhibitor (AZ3146) induced micronuclei by live cell imaging. Intact micronuclei showed expected localization of the compartmentalization markers mRuby-NLS or mRuby-NES, and nucleoplasmic CHMP4B-eGFP (Extended Data Fig. 5c,d, Movie 4,5). Following rupture at sites of nuclear envelope weakness (Fig. 2a arrowhead), CHMP4B was rapidly recruited to discrete foci in proximity of the rupture site (Fig. 2a, Extended Data Fig. 5c,d, Movie 4,5) in a membrane-binding dependent fashion (Fig.

2B, extended data Fig. 5e,f). However, rather than the characteristic transient recruitment associated with successful repair [4,18], CHMP4B progressively spread along the micronuclear envelope followed by persistent accumulation in multiple coalescing foci over hours, without any detectable envelope repair (Fig. 2c, Extended Data Fig. 5c,d Movie 4,5).

Alongside the appearance of CHMP4 foci, we noticed that nuclear envelope morphology rapidly changed from being smoothly round to becoming progressively more convoluted and condensed, most notably at sites of CHMP4B accumulation (Fig. 2d,e, Movie 6). Depletion of CHMP4B or CHMP7 reverted this phenotype (Fig. 2e), suggesting that these morphological changes are dependent on the accumulation of ESCRT-III. CLEM experiments consistently revealed ESCRT-III dependent complex trabecular membrane networks that corresponded to the sites of CHMP4B accumulations in ruptured micronuclei (Fig. 2f, Extended Data Fig. 6, Movie 7). These complex 3-dimensional membrane networks showed striking architectural similarities to the phenotypes observed at primary nuclei upon forced mislocalization of CHMP7 (Extended Data Fig. 7). In fact, micronuclei could accumulate CHMP4B levels comparable to those that drive irreversible rupture of primary nuclei (Fig. 2g). This raises the possibility that excessive ESCRT-III accumulation induces membrane distortion yielding secondary ruptures (Fig. 1g, 2d-f and Extended Data Fig. 4c,e,g). Together, these data show that ESCRT-III is recruited to the envelope of micronuclei upon rupture but is unable to repair the membrane. On the contrary, it accumulates over time and drives micronuclear catastrophe.

We next asked what defects underlie the persistent accumulation of ESCRT-III in the absence of functional repair. Timely recruitment of the VPS4 ATPase (Extended Data Fig. 8a) [1], and exacerbation of CHMP4B accumulation by depletion of the downstream subunit CHMP2A (Extended Data Fig. 8b-d) [27] indicated that ESCRT-III filament turnover remained functional at ruptured micronuclei. In contrast, rupture was associated with a dramatic accumulation of LEMD2 rapidly spreading from the site of rupture to cover the entire micronuclear envelope (Fig. 3a,b, Movie 8), This phenotype required recruitment of CHMP7 (Fig. 3b, Extended Data Fig. 8e, Movie 9). Conversely, CHMP4B accumulation at micronuclei relied on LEMD2 and the presence of the LEMD2 C-terminal CHMP7 interaction domain (Fig. 3c, Extended Data Fig. 8f), indicating a defect in control of nucleation of CHMP4B polymers as the source of the defects at micronuclei.

Accumulation of LEMD2, CHMP7 and CHMP4B (Extended Data Fig. 8g,h) at micronuclei was reminiscent of their interplay at primary nuclei upon ectopic expression of CHMP7^{NES*} (Extended Data Fig. 4f). Considering the delicate balance governing ESCRT-III function [1], this suggested a simple model where micronuclei are unable to limit CHMP7-LEMD2 complex formation to levels required for membrane repair.

To test this hypothesis, we performed *in silico* simulations of nuclear envelope rupture at primary nuclei and micronuclei with parametric ranges inferred from literature, using inner nuclear membrane concentrations of the LEMD2-CHMP7 nucleation complex as readout (Extended Data Fig. 9, materials and methods). Upon rupture, rapid diffusion of cytoplasmic or ER-associated CHMP7 across these small micronuclei rapidly overloaded the pool of LEMD2 along the entire micronuclear envelope (Fig. 3d top panel), while at the much larger primary nuclei CHMP7-LEMD2 accumulation remained restricted to the site of rupture (Fig. 3d bottom panel). When mimicking influx of new LEMD2 molecules upon saturation of available binding sites (Extended Data Fig. 9a), the concentration of LEMD2-CHMP7 complexes at micronuclei far exceeded that at primary nuclei (Fig. 3d), consistent with our observations in cells (Fig. 3a, Movie 9). The simulation experiments postulated that larger micronuclei would be more refractory to LEMD2/CHMP7 complex spreading from the site of rupture and associated CHMP4B accumulation. Indeed, timing CHMP4B spreading along the membrane in relation to micronuclei size in living cells confirmed this prediction (Fig. 3e,f). Finally, low levels of XPO1 suggests that the consequences of CHMP7 influx could be further aggravated in ruptured micronuclei (Fig. 3g, Extended Data Fig. 8i).
Together, our data argue that defects observed at micronuclei can be explained by an inherent inability to restrict CHMP7-LEMD2 complexes, thus licensing unrestrained CHMP4B polymerization and diverting ESCRT-III machinery activity from rapid envelope sealing to persistent membrane distortion.

Considering the ESCRT-III induced morphological changes at primary nuclei and ruptured micronuclei, we explored the relation between ESCRT-III accumulation and the stability of the underlying genome. We exploited ectopic nuclear localization of CHMP7^{NES*} to primary nuclei as a tractable model. CHMP7^{NES*}-induced nuclear ESCRT-III foci were associated with rosettes of

γH2Ax (Extended Data Fig. 10a), and were enriched for the single-stranded DNA (ssDNA)-binding replication protein A2 (RPA2) [28] (Fig. 4a). The fact that RPA2 enrichment was restricted to CHMP4B foci at the nuclear surface (Manders' colocalization coefficient RPA/CHMP4B 0.79 ± 0.23 SD) argued against influx of cytoplasmic stressors underlying this phenotype. Because of the dramatic membrane distortions combined with accumulation of chromatin-associated proteins like LEMD2 [29], we investigated whether RPA2 foci corresponded to areas subject to DNA torsional stress [30]. Strikingly, we found that Topoisomerase IIb (Top2B), the enzyme that relieves torsional stress in chromatin topological domains by transiently generating chromosome breaks [31], was highly enriched at these foci (Fig. 4b and Extended Data Fig. 10b). As Top2B has previously been linked to chromosome rearrangements [31] we tested the consequences of this torsional stress on chromosome integrity by analyzing metaphase spreads following induction of CHMP7 alleles. Whereas overexpression of wild-type CHMP7 induced a low level of DNA breaks, induction of $CHMP7^{NES*}$ dramatically increased the frequency of chromosome breaks and fragmentation (Fig. 4c,d).

Reasoning that this same phenomenon could drive chromosome fragmentation in ruptured micronuclei, we monitored RPA2 accumulation at micronuclei. Indeed, RPA2 colocalized with CHMP4B foci at micronuclei (Fig. 4e, Extended Data Fig. 10c; Manders' colocalization coefficient RPA/CHMP4B 0.94 ± 0.05 SD). Live-cell imaging showed that upon micronuclear rupture RPA2 accumulated rapidly at sites of persistent CHMP4B enrichment along the envelope (Fig. 4f, Movie 10). Micronuclear RPA2 accumulation required unrestrained ESCRT-III driven membrane distortion as depletion of CHMP4B or the CHMP7/LEMD2 nucleation complex suppressed RPA2 accumulation without restoring micronuclear integrity (Fig. 4g, Extended Data Fig. 10g, Movie 10). RPA2 accumulation could be restored by introduction of an siRNA-resistant LEMD2 allele, but not of a $LEMD2^{\Delta C}$ allele unable to recruit CHMP7 and CHMP4B (Fig. 4h, 3c). These data show that unrestrained accumulation of ESCRT-III at primary nuclei and micronuclei has catastrophic effects on the underlying DNA, inducing torsional stress, the generation of ssDNA and chromosome fragmentation.

Taken together our data argue that the LEMD2/CHMP7 compartmentalization sensing mechanism for loss of nuclear envelope integrity is the underlying driver of micronuclear catastrophe. Rupture

of the nuclear envelope permits local nuclear influx of CHMP7 and its association with LEMD2 to license ESCRT-III activation required for sealing (Extended Data Fig. 11). The inherent weakness of this system is evident at the much smaller micronuclei that lack the capacity to restrict CHMP7-LEMD2 complexes to the site of rupture, and instead allow unrestrained activation of ESCRT-III across the surface of the inner membrane (extended data Fig. 11). This phenomenon is associated with dramatic membrane distortion and consequent DNA torsional stress, formation of ssDNA, chromosome damage, as well as the recruitment of exonucleases such as TREX1 (Extended Data Fig. 10d-f) [32,33]. This ultimately drives the fragmentation of chromosomes, possibly in combination with stress ensuing from defective DNA replication and premature chromosome condensation frequently associated with ruptured micronuclei [14,24]. So whereas protein distribution defects predispose micronuclei to rupture, uncontrolled ESCRT-III activity upon rupture precludes their repair and instead drives micronuclear catastrophe and ensuing DNA damage. Therefore, our work highlights the ESCRT-III machinery as a double-edged sword, and suggests that it represents a conditional non-genetic driver of genome instability and the development of cancer.

References and notes:

1. B. E. Mierzwa *et al.*, Dynamic subunit turnover in ESCRT-III assemblies is regulated by Vps4 to mediate membrane remodelling during cytokinesis. *Nat Cell Biol* **19**, 787-798 (2017).
2. J. Schoneberg, I. H. Lee, J. H. Iwasa, J. H. Hurley, Reverse-topology membrane scission by the ESCRT proteins. *Nat Rev Mol Cell Biol* **18**, 5-17 (2017).
3. L. Christ, C. Raiborg, E. M. Wenzel, C. Campsteijn, H. Stenmark, Cellular Functions and Molecular Mechanisms of the ESCRT Membrane-Scission Machinery. *Trends Biochem Sci* **42**, 42-56 (2017).
4. M. Vietri *et al.*, Spastin and ESCRT-III coordinate mitotic spindle disassembly and nuclear envelope sealing. *Nature* **522**, 231-235 (2015).
5. Y. Olmos, A. Perdrix-Rosell, J. G. Carlton, Membrane Binding by CHMP7 Coordinates ESCRT-III-Dependent Nuclear Envelope Reformation. *Curr Biol* **26**, 2635-2641 (2016).
6. M. Gu *et al.*, LEM2 recruits CHMP7 for ESCRT-mediated nuclear envelope closure in fission yeast and human cells. *Proc Natl Acad Sci U S A* **114**, E2166-E2175 (2017).
7. J. Arii *et al.*, ESCRT-III mediates budding across the inner nuclear membrane and regulates its integrity. *Nat Commun* **9**, 3379 (2018).
8. M. D. Stuchell-Brereton *et al.*, ESCRT-III recognition by VPS4 ATPases. *Nature* **449**, 740-744 (2007).
9. H. Y. Fung, S. C. Fu, Y. M. Chook, Nuclear export receptor CRM1 recognizes diverse conformations in nuclear export signals. *Elife* **6**, (2017).
10. K. Kirli *et al.*, A deep proteomics perspective on CRM1-mediated nuclear export and nucleocytoplasmic partitioning. *Elife* **4**, (2015).
11. B. M. Webster *et al.*, Chm7 and Heh1 collaborate to link nuclear pore complex quality control with nuclear envelope sealing. *EMBO J* **35**, 2447-2467 (2016).

12. A. Keppler, H. Pick, C. Arrivoli, H. Vogel, K. Johnsson, Labeling of fusion proteins with synthetic fluorophores in live cells. *Proc Natl Acad Sci U S A* **101**, 9955-9959 (2004).
13. B. M. Webster, P. Colombi, J. Jager, C. P. Lusk, Surveillance of nuclear pore complex assembly by ESCRT-III/Vps4. *Cell* **159**, 388-401 (2014).
14. E. M. Hatch, A. H. Fischer, T. J. Deerinck, M. W. Hetzer, Catastrophic nuclear envelope collapse in cancer cell micronuclei. *Cell* **154**, 47-60 (2013).
15. C. M. Denais *et al.*, Nuclear envelope rupture and repair during cancer cell migration. *Science* **352**, 353-358 (2016).
16. W. H. De Vos *et al.*, Repetitive disruptions of the nuclear envelope invoke temporary loss of cellular compartmentalization in laminopathies. *Hum Mol Genet* **20**, 4175-4186 (2011).
17. Y. Olmos, L. Hodgson, J. Mantell, P. Verkade, J. G. Carlton, ESCRT-III controls nuclear envelope reformation. *Nature* **522**, 236-239 (2015).
18. M. Raab *et al.*, ESCRT III repairs nuclear envelope ruptures during cell migration to limit DNA damage and cell death. *Science* **352**, 359-362 (2016).
19. C. Z. Zhang *et al.*, Chromothripsis from DNA damage in micronuclei. *Nature* **522**, 179-184 (2015).
20. K. J. Mackenzie *et al.*, cGAS surveillance of micronuclei links genome instability to innate immunity. *Nature* **548**, 461-465 (2017).
21. S. M. Harding *et al.*, Mitotic progression following DNA damage enables pattern recognition within micronuclei. *Nature* **548**, 466-470 (2017).
22. S. F. Bakhoum *et al.*, Chromosomal instability drives metastasis through a cytosolic DNA response. *Nature* **553**, 467-472 (2018).
23. S. Liu *et al.*, Nuclear envelope assembly defects link mitotic errors to chromothripsis. *Nature* **561**, 551-555 (2018).
24. K. Crasta *et al.*, DNA breaks and chromosome pulverization from errors in mitosis. *Nature* **482**, 53-58 (2012).
25. J. Willan *et al.*, ESCRT-III is necessary for the integrity of the nuclear envelope in micronuclei but is aberrant at ruptured micronuclear envelopes generating damage. *Oncogenesis* **8**, 29 (2019).
26. A. P. Sagona, I. P. Nezis, H. Stenmark, Association of CHMP4B and autophagy with micronuclei: implications for cataract formation. *Biomed Res Int* **2014**, 974393 (2014).
27. J. Robijns, G. Houthaeve, K. Braeckmans, W. H. De Vos, Loss of Nuclear Envelope Integrity in Aging and Disease. *Int Rev Cell Mol Biol* **336**, 205-222 (2018).
28. R. Chen, M. S. Wold, Replication protein A: single-stranded DNA's first responder: dynamic DNA-interactions allow replication protein A to direct single-strand DNA intermediates into different pathways for synthesis or repair. *Bioessays* **36**, 1156-1161 (2014).
29. A. Brachner, S. Reipert, R. Foisner, J. Gotzmann, LEM2 is a novel MAN1-related inner nuclear membrane protein associated with A-type lamins. *J Cell Sci* **118**, 5797-5810 (2005).
30. I. De Vlaminck *et al.*, Torsional regulation of hRPA-induced unwinding of double-stranded DNA. *Nucleic Acids Res* **38**, 4133-4142 (2010).
31. A. Canela *et al.*, Genome Organization Drives Chromosome Fragility. *Cell* **170**, 507-521 e518 (2017).
32. C. Wolf *et al.*, RPA and Rad51 constitute a cell intrinsic mechanism to protect the cytosol from self DNA. *Nat Commun* **7**, 11752 (2016).
33. J. Maciejowski, Y. Li, N. Bosco, P. J. Campbell, T. de Lange, Chromothripsis and Kataegis Induced by Telomere Crisis. *Cell* **163**, 1641-1654 (2015).

Acknowledgements: We thank U. Dahl Brinch, M. Smestad and L. Kymre for assistance with EM, K. Schink for cell lines, S. Eikvar, E. Rønning, A. Bergersen, and A. Baumeister for technical

support, A. Engen for assistance with cell culture, and C. Bassols for IT support. We also thank V. Nähse, T. Stokke, R. Syljuåsen, T. Liyakat Ali for valuable discussions. The National Core Facility for Human Pluripotent Stem Cells, the Advanced Light Microscopy Core Facility (Oslo University Hospital), the Advanced Electron Microscopy Core Facility (Oslo University Hospital), the Norwegian Advanced Light Microscopy Imaging Network (University of Oslo), and the Section for Cancer Cytogenetics (Oslo University Hospital) are acknowledged for providing facilities. **Funding:** C.C. was supported by the Research Council of Norway (project number 262375). H.S. was supported by the Norwegian Cancer Society (project number 182698) and the South-Eastern Norway Regional Health Authority (project number 2016087). M.V. was supported by the South-Eastern Norway Regional Health Authority (project number 2018043). This work was partly supported by the Research Council of Norway through its Centres of Excellence funding scheme (project number 262652). **Author contributions:** M.V. and C.C. conceived and designed the study with important contributions from H.S. and S.W.S.. M.V. generated cell lines, performed light microscopy, analysed data, and prepared figures. S.W.S. performed and analysed EM experiments, and prepared figures. A.Be. generated cell lines, performed light microscopy, analysed data, and prepared figures. C.M.J. performed and analysed the simulation experiments, and prepared figures. L.I.P. generated cell lines, performed light microscopy, analysed data, and prepared figures. C.R., E.S., E.K., R.T., and A.J. performed light microscopy and analysed data. C.R.J.P. performed metaphase spreads experiments. P.C. provided comments and infrastructure. R.L.K. provided comments and contributed to the simulation setup. S.N.G. and H.K. supervised the simulation experiments. A.Br. supervised and performed EM experiments and provided conceptual input. F.M. supervised and analysed the metaphase spreads experiments. H.S. provided infrastructure and co-supervised the study. C.C. supervised the study, generated constructs and cell lines, performed light microscopy, analysed data, and prepared figures. M.V. and C.C. wrote the paper with contributions from all authors. **Competing interests:** The authors declare no competing interests.

Legends to Figures

Fig. 1| Unrestrained nuclear CHMP7 drives nuclear envelope deformation and rupture. a, Targeting of CHMP4B-mNG foci depend on CHMP7 subcellular localization. RPE1 cell lines stably expressing CHMP4B-mNG were treated with DOX for 2 hours to express the indicated inducible CHMP7-FLAG allele, and with the XPO1 inhibitor leptomycin B (LMB) where indicated, fixed and stained as described. Scale bars, 5 µm. **b,** Nuclear envelope CHMP7 is recruited by LEMD2 and LEMD3. RPE1 cell lines stably expressing CHMP4B-mNG were treated with DOX to express CHMP7-FLAG allele and treated with the indicated siRNA. Number of nuclear envelope CHMP4B foci was monitored by live-cell imaging. Mean and 95% confidence interval are plotted, n> 68, > 33, > 53. **P=0.00379; ***P=0.0007 two-tailed unpaired *t*-test, df=4. **c,** Inactivation of XPO1 drives the formation of nuclear CHMP4B foci. HeLaK CHMP4B-eGFP, mRuby3-NES, LEMD2-SNAP cells were treated with LMB and siRNAs as indicated. CHMP4B foci at the nuclear envelope were monitored by live-cell imaging. Bars, mean and SEM from 3 experiments. Dots, mean from each experiment. n= 116, 281, 258. **P=0.0056 two-tailed unpaired *t*-test, df=4 **d,** Interplay between LEMD2, CHMP4B and CHMP7 at the nuclear envelope. HeLaK CHMP4B-eGFP cells were transfected with mCherry-fusions of the indicated LEMD2 alleles and with $CHMP7^{NES*}$-FLAG where indicated, fixed, stained, processed for confocal imaging and fraction of CHMP4B positive cells was quantified. **e,** Persistent CHMP4B foci colocalize with membrane clusters. HeLaK CHMP4B-eGFP cells stably expressing mCherry-KDEL were transiently transfected with $CHMP7^{NES*}$-FLAG and imaged by live-cell imaging. Scale bars, 5 µm. **f,** CLEM tomography analysis shows that formation of persistent CHMP4B foci results in extensive membrane deformation. HeLaK CHMP4B-eGFP, mRuby3-NES cells were transiently transfected with indicated CHMP7 alleles, followed by imaging, fixation and processing for electron microscopy (top and middle panels). Bottom panels, the tilted representation with modelling of 3 isolated sections of membrane. NUC, nucleus; CYT, cytoplasm. Scale bars, 5 µm. **g,** Overexpression of nuclear CHMP7 results in irreversible membrane rupture. HeLaK CHMP4B-eGFP, mRuby3-NES cells were transfected with indicated constructs and nucleo-cytoplasmic compartmentalization of transfected cells was measured after 24h. Bars, mean and SEM from 3 experiments. n= 217, 172, 180, 102, 88, 62, 82. **P=0.0067; ***P=0.0004 two-tailed unpaired *t*-test, df=4.

Fig. 2| Ruptured micronuclei recruit ESCRT-III and undergo ESCRT-III driven catastrophe. a, CHMP4B persistently accumulated at micronuclei upon rupture. Live-cell imaging of CHMP4B-eGFP, mRuby3-LaminA HeLaK cells treated with AZ3146. Arrowhead indicates weak membrane site. Scale bar, 5 μm. **b,** CHMP4B is recruited to the micronuclear envelope. Micronuclear GFP fluorescence HeLaK cells stably expressing siRNA-resistant CHMP4B-eGFP or the membrane-binding defective mutant CHMP4B^{4DE}-eGFP, treated with CHMP4B siRNA to deplete endogenous CHMP4B and incubated with AZ3146. Bars, mean and SEM from 3 experiments. CHMP4B-eGFP n=24; CHMP4B^{4DE}-eGFP n=22. ***P=0.0001 two-tailed Mann Whitney Test. **c,** HeLaK or RPE1 CHMP4B-eGFP, mRuby3-NLS cells were treated with AZ3146 to induce formation of micronuclei, and stained with SiR-Hoechst. Micronuclei repair events and persistence of CHMP4B foci at ruptured micronuclei were monitored by live-cell imaging. Bars, mean and SEM from 3 experiments. n= 139, 90, 138, 72. *P=0.046 two-tailed unpaired *t*-test, df = 4. **d,** Micronuclear CHMP4B foci correspond to convoluted envelope regions. Wide field image of live micronucleated HeLaK CHMP4B-eGFP, mCherry-KDEL cells stained with SiR-Hoechst. Scale bar, 5 μm. **e,** CHMP4B accumulation results in collapse of the micronuclear envelope. HeLaK CHMP4B-eGFP, mCherry-KDEL cells were treated with indicated siRNAs, and micronuclei were monitored by live-cell imaging for rupture events. Micronuclear circularity was measured before rupture and 60 minute after rupture, with circularity a proxy for membrane deformation. Bars indicate mean and SEM from 3 experiments. n=16 each condition. ***P <0.0001, **P=0.0024 paired *t*-test, df= 4. **g,** Aberrant accumulation of CHMP4B at ruptured micronuclei resembles CHMP7^{NES*}- induced accumulations at primary nuclei. CHMP4B intensity was measured in live RPE1 cells during nuclear envelope reassembly (anaphase), in ruptured micronuclei (MN) and in CHMP7^{NES*} DOX-induced foci at primary nuclei (PN DOX+). Bars, mean and SEM from 3 experiments. n= 37, 41, 30. ****P<0.0001, df=76, 65. .*P=0.0343 df=69, two-tailed unpaired *t*-test with Welch correction. **f,** CHMP4B hyperaccumulation at ruptured micronuclei induces membrane deformations similar to those observed at primary nuclei. HeLaK CHMP4B-eGFP, mRuby3-NES cells were treated with indicated siRNAs, incubated with AZ3146 to induce micronuclei, fixed and imaged by confocal microscopy to identify ruptured micronuclei. Samples were processed for correlative electron

microscopy. A 3D-model of the micronuclear envelope was built from electron tomography of an untreated ruptured micronucleus (left panel).

Fig. 3| Ruptured micronuclei lack the ability to restrain ESCRT-III activity. a, LEMD2 hyperaccumulates at micronuclei upon rupture. HeLaK mRuby3-NES, LEMD2-SNAP cells were treated with AZ3146 to induce formation of micronuclei, stained with SiR-SNAP, and events at micronuclei were monitored by live cell imaging. Scale bar, 5 µm. **b,** LEMD2 hyperaccumulation depends on CHMP7 and CHMP4B. As in panel d, but including treatment with indicated siRNAs. LEMD2 intensity at the micronuclear envelope was monitored by live-cell imaging, intensity fold increase 60 minutes after rupture was quantified and plotted. Intensity changes in mCherry-KDEL are included as reference. Bars indicate mean and SEM of 3 experiments for LEMD2, mean and 95% confidence interval for KDEL. n=15, 16, 15, 17. ***P=0.0001 two-tailed unpaired *t*-test with Welch's correction. **c,** CHMP4B recruitment at ruptured micronuclei depends on LEMD2. CHMP4B recruitment at ruptured micronuclei was monitored in HeLaK CHMP4B-eGFP, mCherry-KDEL, SNAP-RPA2 cells treated with the indicated siRNA and expressing the indicated LEMD2 rescue alleles. ΔC lacks the C-terminal CHMP7 interaction surface. Bars, mean and SEM from 3 experiments. n= 44, 51, 40, 44. ****P<0.0001 two-tailed unpaired *t*-test, df=6. **d,** CHMP7-LEMD2 complex accumulation along the inner envelope membrane of micronuclei (top panels) and primary nuclei (bottom panels) following rupture. Simulation experiments describing interaction dynamics of cytoplasmic CHMP7 and inner nuclear membrane-bound LEMD2 in primary nuclei (400 μm^3) and micronuclei (4 μm^3) at different time points following envelope rupture (100nm, at the north pole, indicated by arrowhead) while considering influx of novel LEMD2 molecules (maximum occupancy fraction 0.5; extended data Fig. 7a). A five-color heatmap was used to visualize the local density of CHMP7-LEMD2 complexes along the inner nuclear membrane, as a function of the angle from the pore (located at the top of the figure). The parameters used for simulations are described in the Materials and Methods section. Scale bars, 1 µm. **e,** Time of CHMP4B spreading across the micronucleus in micronuclei with different diameter upon rupture in CHMP4B-eGFP, mRuby2-NLS, SiR-Hoechst. Whiskers, 5-95% percentile. n= 19, 27, 31. *P=0.011, **P=0.0007, two-tailed unpaired *t*-test, df=4. **f,** CHMP4B accumulation rate depends on micronuclei size. Live-cell imaging of rupturing micronuclei of different diameters in

CHMP4B-eGFP, mCherry-KDEL HeLaK cells treated with AZ3146 . Scale bars, 5 µm. **g,** Ruptured micronuclei lose the capacity to retain XPO1. XPO1 levels in intact or ruptured primary nuclei (PN) and micronuclei (MN) of CHMP4B-eGFP HeLa cells fixed and stained for endogenous XPO1. Bars, mean and SEM of 3 experiments. n= 113, 66, 15, 35. *P=0.04, **P=0.001, two-tailed unpaired *t*-test df=4.

Fig. 4| Unrestrained CHMP7 drives DNA damage, torsional stress and chromosome fragmentation. a, Nuclear CHMP4B foci associate with the ssDNA marker RPA2. RPE1 CHMP4B-mNG, mRuby3-NES and inducible CHMP7-FLAG or CHMP7^{NES*}-FLAG cells were treated with DOX to induce the indicated CHMP7 allele, fixed, stained for RPA2 and imaged by Airyscan microscopy. Nuclei are outlined. An Imaris surface 3D-rendering (right panel) of RPA2 foci localizing at or in close proximity to CHMP4B foci at the surface of the primary nucleus (inset). For n=12 primary nuclei, Manders' colocalization coefficient RPA/CHMP4B 0.79 ± 0.23. Scale bars, 5 µm and 0.3 µm (Imaris reconstruction). **b,** Nuclear CHMP7 induces DNA torsional stress. CHMP4B-mNG, mRuby3-NES and inducible CHMP7-FLAG or CHMP7^{NES*}-FLAG RPE1 cells were treated with DOX to induce the indicated CHMP7 allele, fixed, stained for Top2B and imaged by confocal microscopy. The number of nuclear foci of TOP2B was quantified. Bars, mean and SEM. n=255, 136, 205. ****P < 0.0001 two-tailed Mann Whitney Test. **c,** Nuclear CHMP7 drives chromosome breaks and fragmentation. RPE1 mRuby3-NES and inducible CHMP7-FLAG or CHMP7^{NES*}-FLAG cells were treated with DOX to induce the indicated CHMP7 allele, incubated overnight with colchicine and processed for cell harvesting and metaphase spread analysis. Bars, mean and SEM. ****P < 0.0001 two-tailed Mann-Whitney test. **d,** Representative examples of the experiments described in panel C. **e,** CHMP4B colocalizes with RPA2 at ruptured micronuclei. HeLaK cells were treated with AZ3146 to induce micronuclei, fixed, stained as indicated and imaged by Airyscan microscopy. CHMP4B and RPA2 show a strong spatial correlation. For n=14 micronuclei, Pearson's correlation 0.84 ± 0.15; Manders' colocalization coefficient RPA/CHMP4B 0.94 ± 0.05. Right panel, Imaris surface 3D-rendering. Scale bars, 5 µm and 0.5 µm (Imaris reconstruction). **f,** RPA2 enrichment at ruptured micronuclei follows CHMP4B foci formation. HeLaK CHMP4B-eGFP, mRuby3-NES, RPA2-SNAP cells were incubated with AZ3146, stained with SiR-SNAP, and resulting micronuclei were monitored by

live-cell imaging. Accumulation of RPA2 is indicated relative to time of rupture. Arrowhead indicates a rupturing micronucleus. Scale bar, 5 µm. **g,** RPA accumulation at ruptured micronuclei requires ESCRT-III. HeLaK CHMP4B-eGFP, mRuby3-NES, RPA2-SNAP cells were treated with indicated siRNAs, incubated with AZ3146, stained with SiR-SNAP and resulting micronuclei were monitored every 5 min by live-cell imaging. Micronuclei were considered RPA2-positive when RPA enrichment was observed following rupture, and fraction of RPA2-positive ruptured micronuclei is plotted over time. Mean (line) and SEM (bands) are indicated. Con n=41; CHMP2A n=46; CHMP4B n=43; CHMP7+LEMD2 n=27. ****P< 0.0001 two-tailed unpaired *t*-test. Df=8 (CHMP4B vs Con); Df=7 (CHMP7+LEMD2 vs Con). **h,** RPA accumulation at ruptured micronuclei requires LEMD2 C-terminus. As in g, RPA2 accumulation was monitored in parental cells or upon stable expression of the indicated LEMD2 rescue alleles. Mean and SEM from three experiments are indicated. n= 36, 42, 27, 40. ***P=0.0003, **P=0.0085, two-tailed unpaired *t*-test, df=6.

Legends to Extended Data Figures

Extended Data Fig. 1| Nuclear localization of CHMP7 regulates ESCRT-III activation at the nuclear envelope. a, A CHMP7 c-terminal motif can function as a NES. HeLaK cells were transfected with REV(1.4)-eGFP fusions with aa 421-430 of CHMP7 that constitute a predicted NES, or a mutated version of this sequence (NES*; L421A, L425A, L428A triple mutation), followed by live-cell microscopy. LMB was added where indicated. SiR-Hoechst (red), DNA. Quantification in Extended Data Fig. 1c. Scale bars, 5 µm. **b,** Quantification of subcellular localization of REV(1.4)-eGFP fusions as shown in Fig. 1d. LMB treatment where indicated. Bars, SEM, dots represent the mean of each independent experiment. n= 218, 149, 138, 153 cells. ****P<0.0001, two-tailed unpaired t-test, df=4. **c,** CHMP7 contains a putative NES. CHMP7 domain structure and sequence alignment of CHMP7 from multiple eukaryotes compared to MIM1 (MIT-interacting motif 1) and type 1a NES consensus sequences. Human (hs), mouse (mm), drosophila (dm), budding yeast (sc), slime mold (dicdi). Conserved residues are shaded. **d,** Schematic representation of human CHMP7 functional domains and mutant alleles used in this study. **e,** RPE1 CHMP4B-mNG, mRuby3-NES, CHMP7^{NES*}-FLAG cells treated with DOX to induce CHMP7^{NES*}-FLAG overexpression. Immunoblot of whole-cell lysates shows CHMP7^{NES*}-FLAG levels at indicated time points after DOX addition. **f,** As in e, quantification of CHMP4B foci. Bars, mean and SEM from 3 experiments. n=30 each time point. **P<0.05, ***P<0.0001 two-tailed unpaired *t*-test with Welch correction. **g,** RPE1 CHMP4B-mNG, mRuby3-NES, CHMP7^{NES*}-FLAG cells treated with DOX to induce CHMP7^{NES*}-FLAG overexpression. Immunoblot of whole-cell lysates shows CHMP7^{NES*}-FLAG levels at indicated time points after DOX wash out. **h,** As in g, quantification of CHMP4B nuclear envelope foci, CHMP7^{NES*}-FLAG mRNA and CHMP7^{NES*}-FLAG protein levels before (PRE) DOX induction and following DOX wash out. Bars, SEM. Dots for bar graphs represent the mean of 3 independent experiment; dots for dotplot represent individual measurements, n= 65, 73, 65, 74, 64. ****P<0.0001; ***P<0.001, Dunnett's multiple comparison test compares time points of each parameter to the corresponding pre-DOX. **i,** As in g, representative confocal images showing CHMP4B-eGFP nuclear envelope foci. Scale bars, 10 µm.

Extended Data Fig. 2| Interplay between CHMP7 and XPO1 activity. a, Inactivation of XPO1 drives the formation of nuclear CHMP4B foci. HeLaK CHMP4B-eGFP, mRuby3-NES, LEMD2-SNAP cells were treated with LMB and CHMP4B localization was monitored by live-cell imaging, with time after start of imaging indicated. Scale bar, 5 μm. **b,** ESCRT-III nuclear envelope foci induced by LMB treatment were monitored every 30 min by live-cell imaging in HeLaK CHMP4B-eGFP, mRuby3-NES, LEMD2-SNAP cells after LMB wash out. Mean and 95% confidence interval are plotted. n=23 cells from 16 movies. **c,** Formation of CHMP4B nuclear envelope foci upon XPO1 inactivation was monitored in live HeLaK CHMP4B-eGFP, mRuby3-NES, LEMD2-SNAP cells were treated with indicated siRNAs and LMB where indicated. CHMP4B foci formation depended on CHMP7. Scale bar, 5 μm. **d,** Immunoblot of whole-cell lysate showing depletion of endogenous CHMP7 upon siRNA treatment.

Extended Data Fig. 3| Nuclear localization of CHMP7 stabilizes LEMD2-CHMP7-CHMP4B complexes at the nuclear envelope. a, LEMD2 overexpression selectively depletes CHMP4B levels. HeLaK CHMP4B-eGFP, LEMD2-mCherry cells were treated with DOX to induce overexpression of LEMD2 and were subsequently monitored by live-cell imaging. Scale bar, 5 μm. **b,** LEMD2 overexpression dependent depletion of CHMP4B is countered by co-overexpression of CHMP7. Wide-field images of live HeLaK CHMP4B-eGFP cells transiently transfected with the indicated alleles. Transfected cells are outlined. Scale bar, 5 μm. **c,** Schematic representation of LEMD2 functional domains and deletions used in this study. LEM, LAP2, Emerin, MAN1 domain. TM, transmembrane domain; MSC, MAN1-Src1p C-terminal domain. **d,** Interplay between LEMD2, CHMP4B and CHMP7 at the nuclear envelope. HeLaK CHMP4B-eGFP cells were transfected with mCherry-fusions of the indicated LEMD2 alleles and with $CHMP7^{NES*}$-FLAG where indicated, fixed, stained and processed for confocal imaging. Outlines are drawn around mCherry positive cells, and the inset is show in the right-hand panel. Scale bar, 5 μm. **e,** LEMD2 overexpression selectively depletes CHMP4B levels. Quantification of CHMP4B intensity in HeLaK CHMP4B-eGFP cells transiently transfected with the indicated mCherry fusion alleles and imaged live. Bars, mean and SEM from 3 experiments. n= 211, 179, 119, 107, 92, 40. ****P<0.0001 and ***P=0.0006 two tailed unpaired *t*-test. df=4. **f,** Quantification of CHMP4B intensity in HeLaK CHMP4B-eGFP cells transfected with mCherry fusions of the indicated

LEMD2 alleles and imaged live. Bars, mean and SEM from 3 experiments. n= 145, 67, 166, 111. ***P=0.0001 two-tailed unpaired *t*-test, df=4.

Extended Data Fig. 4| Unrestrained nuclear CHMP7 drives nuclear envelope deformation and rupture. a, Persistent CHMP4B foci colocalize with membrane clusters but not NPCs. Wide-field images of live HeLaK CHMP4B-eGFP and mCherry-Lap2β, or mCherry-NUP58 cells were transiently transfected with CHMP7^{NES*}-FLAG. Images show a projection of 3 z-planes Scale bars, 5 µm. **b,** CLEM tomography analysis showing that formation of persistent CMP4B foci results in extensive membrane deformation. HeLaK CHMP4B-eGFP, mRuby3-NES cells were treated with DOX for 6 hours to induce CHMP7^{NES*}-FLAG. Formation of CHMP4B foci and loss of nucleo-cytoplasmic compartmentalization were monitored in live cells. **c,** Overexpression of nuclear CHMP7 results in irreversible membrane rupture. RPE1 CHMP4B-mNG, mRuby3-NES and inducible CHMP7-FLAG, CHMP7^{NES*}-FLAG or CHMP7^{2NLS}-FLAG cells were treated with DOX to induce the indicated CHMP7 allele and monitored in live-cell imaging. Nuclear compartmentalization was assessed by measuring nucleus/ cytoplasm ratio of mRuby3-NES and plotted. Bars, mean and SEM from 3 experiments. n= 101, 108, 125, 138, 129, 108. two-tailed *t*-test CHMP7^{NES*} DOX-/+ **P= 0.0074, df=4; CHMP7^{NLS} DOX-/+ **P= 0.0054 df=4, CHMP7 DOX+/ CHMP7^{NES*} DOX+ *P=0.0212 df=4; CHMP7 DOX+/ CHMP7^{NLS} DOX+ *P=0.0117. **d,** Immunoblot from whole cell lysates showing expression of endogenous CHMP7 and DOX -induced CHMP7 alleles. **e,** Quantification of nucleo-cytoplasmic compartmentalization. in RPE1 CHMP4B-mNG, mRuby3-NES, CHMP7^{NES*}-FLAG cells treated with DOX to induce CHMP7^{NES*}-FLAG overexpression. Bars, mean and SEM from 3 experiments. n=30 each time point. **P=0.0073, ***P<0.0001, two-tailed unpaired t-test with Welch correction, df=29.61, 29.97, 29.25. **f,** Overexpression of nuclear CHMP7 drives formation of LEMD2-CHMP4B nuclear envelope foci. Images of live HeLaK CHMP4B-eGFP, mRuby3-NES and LEMD2-SNAP cells transiently transfected with the indicated CHMP7 alleles and labelled with SiR-SNAP. Nucleus perimeter is outlined. Scale bars, 5 µm. **g,** LEMD2 and LEMD3 recruit ESCRT-III at the nuclear envelope. Nuclear-cytoplasmic compartmentalization was monitored in CHMP4B-eGFP, 2xmRuby3-NES cells, treated with DOX to induced CHMP7^{NES*}-FLAG and formation of nuclear envelope ESCRT-III foci and transfected with the indicated siRNA. Bars, mean and 95% confidence interval. n= 30 each sample. **P=0.0025, 8P=0.024 two-tailed unpaired *t*-test, df=4.

Extended Data Fig. 5| ESCRT-III is recruited at micronuclei upon rupture. a, CHMP4B localization at ruptured micronuclei in different cell lines. Cells were treated with AZ3146, fixed and stained for endogenous CHMP4B and the nuclear envelope marker Emerin. Scale bars, 5 µm. **b,** ESCRT-III complex subunits and effectors localize at micronuclei. Confocal images of micronuclei from HeLaK cells fixed and immunolabelled for the indicated endogenous factors. Scale bars, 1 µm. **c,** CHMP4B persistently accumulated at micronuclei upon rupture.HeLaK CHMP4B-eGFP, mRuby3-NLS cells were treated with AZ3146 to induce formation of micronuclei, stained with SiR-Hoechst, and events at micronuclei were monitored by live cell imaging. Scale bar, 5 µm. **d,** HeLaK CHMP4B-eGFP, mRuby3-NES cells were treated with AZ3146 to induce formation of micronuclei, stained with SiR-Hoechst, and events at micronuclei were monitored by live cell imaging. Arrowheads indicate a rupturing micronucleus. Scale bar, 5 µm. **e,** CHMP4B is recruited to the micronuclear envelope. Confocal microscopy of HeLaK cells stably expressing siRNA-resistant CHMP4B-eGFP or the membrane-binding defective mutant CHMP4B^{4DE}-eGFP, treated with CHMP4B siRNA to deplete endogenous CHMP4B and incubated with AZ3146. Insets show micronuclei. Scale bars, 5 µm. **f,** As in e, immunoblot of whole-cell lysate showing depletion of endogenous CHMP4B and expression of the eGFP-fusions.

Extended Data Fig. 6| ESCRT-III drives extensive membrane deformations in ruptured micronuclei. a, Micronuclear CHMP4B foci correspond to areas of extreme membrane deformations. CLEM of a HeLaK CHMP4B-eGFP cell, treated with AZ3146 to induce micronuclei, fixed, imaged with confocal microscopy and then processed for EM. Position of CHMP4B foci (detected by light microscopy) relative to areas of the micronuclei where the nuclear envelope is dramatically deformed (observed on consecutive EM sections). Subsequent confocal planes with the respective electron micrographs are shown. Arrowheads indicate confocal planes of CHMP4B-eGFP foci and the corresponding areas in the electron micrographs. Asterisks mark are included as reference for micronuclei position. **b,** CHMP4B foci (detected by light microscopy) correlate with micronuclear envelope deformations (arrowheads) in naturally occurring micronuclei (observed on EM sections, arrowheads) of HeLaK CHMP4B-eGFP cells. **c,** Endogenous CHMP4B foci (detected by light microscopy) correlate with micronuclear envelope deformations (arrowheads) in micronuclei (observed on tomograms from consecutive EM

sections) of HeLaK cells. **d,** ESCRT-III depletion rescues micronuclear envelope trabecular distortions. CLEM of ruptured micronuclei in HeLaK CHMP4B-eGFP, mRuby3-NES cells transfected with indicated siRNAs, incubated with AZ3146, fixed, imaged with light microscopy and processed for EM.

Extended Data Fig. 7| Ruptured micronuclei ultrastructure resemble trabecular membrane network driven by CHMP7 overexpression. Electron tomograms from CLEM experiments and 3D-models of membrane ultrastructure induced by overexpression of $CHMP7^{NLS}$-FLAG (upper panels) or $CHMP7^{NES*}$-FLAG (middle panels). Note the similarity to a "spontaneously" ruptured micronuclei of HeLaK cells with distinct endogenous CHMP4B foci (from Extended Data Fig. 5c) (lower panels).CYT, cytoplasm; NUC, nucleoplasm.

Extended Data Fig. 8| Micronuclei are unable to restrict CHMP7-LEMD2 complexes. a, VPS4 is recruited at ruptured micronuclei with similar kinetics as CHMP4B. Live-cell imaging of CHMP4B-eGFP, VPS4A-SNAP, mRuby3-NLS cells. Scale bar, 5 μm. Representative of n=41, 3 experiments. **b,** CHMP2A depletion aggravates micronuclei collapse phenotypes. Wide-field images of ruptured live CHMP4B-eGFP, mCherry-KDEL HeLa cells treated with AZ3146 and siRNAs as indicated. Scale bars, 5 μm. **c,** As in b, cells were fixed, imaged by confocal microscopy and CHMP4B accumulation at ruptured micronuclei was measured. Bars, mean and SEM. n= 39, 53. **P= 0.003 two-tailed unpaired *t*-test, df=4. **d,** As, in C Immunoblot of whole-cell lysate of HeLaK CHMP4B-eGFP cells showing efficient depletion of CHMP2A upon siRNA treatment. **e,** LEMD2 is hyper-recruited at micronuclei upon rupture and in a CHMP7-dependent fashion. LEMD2 intensity was monitored in live-cell imaging of HeLaK CHMP4B-eGFP, mRuby3-NES and LEMD2-SNAP cells, transfected with indicated siRNA and labelled with SiR-SNAP. Localization of mRuby3-NES was used to determine rupture time. Scale bars, 5 μm. **f,** As in Fig. 3d, immunoblot from whole cell lysate showing efficient depletion of endogenous LEMD2 and expression of rescue alleles. **g,** CHMP4B, LEMD2 and CHMP7 enrich at a fraction of micronuclei. HeLaK CHMP4B-eGFP cells were treated with AZ3146 fixed, stained as indicated and imaged by Airyscan microscopy. **h,** As in g, quantification of the fraction of micronuclei enriched in CHMP4B-eGFP, endogenous LEMD2 and CHMP7 as in Fig. 3c. Bars, mean and SEM from 3 experiments, n=2666 micronuclei. **i,** micronuclei lack the buffering capacity to retain XPO1.

Confocal imaging of micronucleated CHMP4B-eGFP, mRuby3-NES HelaK cells, treated with DOX to induce CHMP7^{NES*}, fixed and stained for XPO1 and Hoechst. Asterisk indicates a ruptured primary nucleus. Arrowheads indicates a ruptured micronucleus. Scale bar, 5 μm.

Extended Data Fig. 9| Micronuclei are unable to restrict CHMP7-LEMD2 complexes. a, Phi line plots from *in silico* experiments showing evolution of CHMP7-LEMD2 complex angular density along the INM from the rupture site (φ to pore = 0) to the opposite pole (φ to pore = π) for cytoplasmic CHMP7. Results are shown for micronuclei (top panel) and primary nuclei (bottom panel) at different time points after rupture (as indicated), and using different LEMD2 occupancy cut-offs for generation of new INM LEMD2 molecules. **b,** as Fig. 3h, but with CHMP7 as an ER membrane-bound protein. **c,** as A, but with CHMP7 as an ER membrane-bound protein.

Extended Data Fig. 10| Unrestrained nuclear ESCRT-III and its consequences for the genome. a, Nuclear CHMP4B foci associate with local DNA damage. RPE1 CHMP4B-mNG, mRuby3-NES and inducible CHMP7-FLAG, CHMP7^{NES*}-FLAG or CHMP7-ΔN^{NES*}-FLAG (unable to bind to membranes) were treated with DOX, fixed and stained for the DNA damage marker γH2Ax. Scale bars, 5 μm. **b,** Nuclear CHMP7 induces DNA torsional stress. RPE1 CHMP4B-mNG, mRuby3-NES and inducible CHMP7-FLAG or CHMP7^{NES*}-FLAG cells were treated with DOX to induce the indicated CHMP7 allele, fixed, stained for Top2B and imaged by confocal microscopy. Quantification of Top2B accumulation in Fig. 4b. Scale bars, 5 μm. **c,** CHMP4B intensity at micronuclei correlates with RPA accumulation. Fixed HeLaK cells were immunolabelled for CHMP4B and RPA2. RPA2 and CHMP4B fluorescence intensities were measured within the same micronuclei and plotted on the x- and y-axes, respectively. Regression line (line) and 95% confidence interval (bands) are indicated. R^2= 0.4978, n= 31. **d,** The ER-associated TREX1 exonuclease enriches at nuclear CHMP4B foci. RPE1 CHMP4B-mNG, mRuby3-NES and inducible CHMP7-FLAG or CHMP7^{NES*}-FLAG cells were treated with DOX to induce the indicated CHMP7 allele, fixed, stained for TREX1 and imaged by confocal microscopy. Scale bars, 5 μm. **e,** TREX1 is enriched at CHMP4B foci in collapsed micronuclei. CHMP4B-eGFP, mRuby3-NES, RPA2-SNAP HeLaK cells were treated with AZ3146 to induce micronuclei, fixed and stained for RPA2 and TREX1. Scale bar, 5 μm. **f,** Quantification of ruptured micronuclei showing TREX1 enrichment. mRuby3-NES, CHMP4B-eGFP HeLaK cells were

treated with Control siRNA or a CHMP4B siRNA targeting both endogenous and GFP-tagged allele. Cells were then treated with AZ3146 to induce formation of micronuclei, fixed and stained for TREX1. Bars indicate mean and SEM, dots represent the mean of each independent experiment. Con, n=171; CHMP4B, n=238. **P=0.0025 two-tailed unpaired *t*-test, df=4. **g,** Immunoblot from whole-cell lysate showing efficient depletion of endogenous proteins.

Extended Data Fig. 11| Model for ESCRT-III function at nuclear envelope of primary nuclei and micronuclei. When the nuclear envelope is intact (steady state) CHMP7 is continuously exported from the nucleus in an XPO1-dependent fashion, precluding its interaction with LEMD2 at the INM. Upon rupture, CHMP7 freely diffuses into the nucleus through the site of rupture. LEMD2-CHMP7 complexes form in proximity of the rupture site to activate ESCRT-III polymerization and sealing activity (repair). micronuclei are intrinsically unable to restrain ESCRT-III activity. Upon rupture, CHMP7 diffuses into the micronuclei, quickly spreads along the whole INM surface and rapidly saturates all available LEMD2. This lack of CHMP7-LEMD2 restriction causes unrestrained ESCRT-III activity that is unable to repair the membrane and instead drives extreme membrane deformation, micronuclei catastrophe and DNA damage. The bar at the bottom of each illustration represents the cytosolic vs (micro)nuclear distribution of CHMP7.

Legends to Movies

Movie 1. Formation of nuclear CHMP4B-LAP-eGFP foci upon treatment with Lemptomycin B.

Movie 2. Doxycycline-induced expression of LEMD2-SNAP induces depletion of cellular CHMP4B-LAP-eGFP.

Movie 3. Doxycycline-induced expression of CHMP7^{NES*}-V5 induces formation of nuclear CHMP4B-LAP-mNG-3HA foci followed by nuclear envelope rupture (as assessed by 2xmRuby3-NES) in interphase cells.

Movie 4. Persistent accumulation of CHMP4B-LAP-eGFP at micronuclei following rupture, assessed by 2xmRuby3-NES nuclear influx.

Movie 5. Persistent accumulation of CHMP4B-LAP-eGFP at micronuclei following rupture, assessed by mCherry-NLS nuclear efflux.

Movie 6. CHMP4B-LAP-eGFP accumulation induces distortion of micronuclear membranes, as assessed by mCherry-KDEL.

Movie 7. Electron tomogram of a CHMP4B-positive ruptured micronucleus showing extensive trabecular membrane deformation.

Movie 8. LEMD2-SNAP spreading and accumulation at micronuclei following rupture.

Movie 9. LEMD2-SNAP spreading and accumulation at micronuclei following rupture upon treatment with siRNA targeting CHMP4B or CHMP7.

Movie 10. Accumulation of SNAP-RPA2 at sites of persistent CHMP4B enrichment requires CHMP4B, CHMP7, and LEMD2. Live-cell imaging of HeLaK CHMP4B-eGFP (green),

mRuby3-NES (cyan) and RPA2-SNAP (red) treated with AZ3146 and labelled with SiR-SNAP. Circles in frame 1 indicate rupturing micronuclei.

Materials and Methods

Cell cultures

Cell lines were cultured as recommended by ATCC guidelines. For live-cell imaging, cells were seeded into glass bottom imaging dishes (Lab-Tek, Nunc; MatTek, MatTek Corporation). For immunofluorescence studies, cells were grown on high Precision cover glass (Marienfeld). For confocal microscopy, cells were fixed with 4% EM grade Formaldehyde (Polysciences) for 5 minutes at 37 ℃. Cells were then permeabilized by treatment with 0.16% Triton X-100 for 2 minutes. Primary and secondary antibodies were diluted in PBS/0.05% Saponin and incubated for 1 to 2 hours. After antibody staining, samples were mounted on microscope slides (Menzel-Glaser) with Mowiol for standard confocal imaging or SlowFade Gold Antifade Reagent (Life Technologies) for Airyscan microscopy. RPE1 and HeLaK cell lines stably expressing inducible CHMP7 or LEMD2 alleles were treated with 500 ng/ml doxycycline (DOX, Sigma-Aldrich). XPO1 inhibition was carried on by incubating cells with 2.5 ng/ml Leptomycin B (LMB, InvivoGen) for up to 3 hours. Loss of XPO1 activity was monitored my nuclear localization of 2xmRuby3-NES. Micronucleation was induced by MPS1 inhibitor AZ3146 (Selleckcem) used at a concentration of 2 μM. RPE1 cell lines were depleted for p53 before AZ3146 treatment.

Stable cell lines

A stable HeLa "Kyoto" cell line expressing CHMP4B-eGFP was obtained from Anthony Hyman[34]. All other stable cell lines were lentivirus-generated pools. To achieve low expression levels, the weak PGK promoter was used for transgene expression. For higher expression levels CMV or EF1α promoters were used. Third generation Lentivirus was generated using procedures and plasmids as previously described[35]. Briefly, (eGFP/mNG/mCherry/SNAP/FLAG fusions of) transgenes were generated as Gateway ENTRY plasmids using standard molecular biology techniques, with all CHMP4B-fusions containing the LAPtag module[34]. From these vectors, Lentiviral transfer vectors were generated by recombination into lentiviral destination vectors (Addgene plasmids # 19067, 19068, 41393; and vectors derived from pCDH-EF1α-MCS-IRES-PURO (SystemBiosciences, inc.)) using Gateway LR reactions. VSV-G pseudotyped lentiviral particles were packaged using a third generation packaging system[36] (Addgene plasmids # 12251, 12253, 12259). HeLaK or RPE1 cells were then transduced with low virus titers (MOI ≤1) and

stable expressing populations were generated by antibiotic selection. Detailed cloning procedures are available on request. The stable cell lines used in this study are listed in Table 2.

Transient plasmid transfections

For transient expression of CHMP7 and LEMD2 alleles, cells were grown on Precision cover glass in 24-well plates or into glass bottom imaging dishes and transfected with 0.5 μg DNA construct complexed with Fugene6 (Promega) following the manufacturer's instruction. Cell were then fixed or imaged by live-cell imaging 12 to 24 hours after transfection. Non-targeting control Silencer Select siRNA (pre-designed, Cat. No. 4390844) was used as control. The plasmids used in this study are listed in Table 2, and detailed cloning procedures are available on request.

siRNA transfections

All siRNAs were purchased from Ambion and contained the Silencer Select modification. Cells at 50% confluency were transfected with Lipofectamine RNAiMAX transfection reagent (Life Technologies) following the manufacturer's instruction. Cells were transfected with 50 nM CHMP2A siRNA (AAGAUGAAGAGGAGAGUGAtt) or p53 (GUAAUCUACUGGGACGGAAtt) for 48 hours. CHMP4B (CAUCGAGUUCCAGCGGGAGtt), CHMP7 (AGGUCUCUCCAGUCAAUGAtt) and LEMD2 (AGCUGGUAAUUUUGAGUGUtt) were silenced by 2x serial transfections with 50 nM siRNA concentration for a total of 72 hours.

Antibodies

Rabbit anti-human CHMP4B antibody (WB 1:2000, IF 1:1000) and rabbit anti-CHMP3 (IF 1:1000) were produced as previously described[37,38]. Rabbit anti-CHMP2A (Proteintech #10477-1-AP; WB 1:500, IF 1:100), rabbit anti-CHMP7 (Proteintech #16424-1-AP; Sigma-Aldrich; WB 1:250), mouse anti-CHMP7 (Abnova #H00091782-B01; IF 1:100), rabbit anti-LEMD2 (Abnova #PAB20940; WB 1:500; IF 1:100), mouse anti-CHMP1A (Abcam, #ab104100; IF 1:150), rabbit anti-VPS4 (Sigma-Aldrich #SAB4200025; WB 1:500, IF 1:200), mouse anti-γH2Ax (Millipore 05-636; IF 1:100), mouse anti-Emerin (NeoMarkers MS-1751; IF 1:100), mouse anti-RPA2 (Abcam #ab2175; IF 1:100), rabbit anti-TREX1 (Abcam #ab185228; IF 1:200), mouse anti-TOP2B (scbt #sc-25330; IF 1:200), mouse anti-β-Actin (Sigma-Aldrich; WB

1:30000), mouse anti-GFP (Roche #1814460001; WB 1:1000; IF 1:200), rabbit anti-FLAG (Cell Signaling Technology 2368; WB 1:1000; IF 1:400), rabbit anti-Histone H3 (Abcam #ab1791; WB 1:10000) and mouse anti-Lamin B1 (scbt #sc365962; WB 1:1000) were used as primary antibodies. DNA was labelled with Hoechst 33342 (2 µg/ml, Life Technologies. Secondary antibodies included anti-mouse-, anti-rabbit- and anti-goat- Alexa488 (Jackson), Alexa568 (molecular Probes) and Alexa647 (Jackson).

Confocal microscopy

Fixed samples were imaged with a Zeiss LSM 710 or 780 confocal microscope (Carl Zeiss MicroImaging GmbH, Jena, Germany) equipped with an Ar-Laser Multiline (458/488/514 nm), a DPSS-561 10 (561 nm), a Laser diode 405-30 CW (405 nm), and a HeNe-laser (633 nm). The objective used was a Zeiss Plan-Apochromat 63x/1.40 Oil DIC M27. Image processing was performed with basic software ZEN 2009 (Carl Zeiss MicroImaging GmbH, Jena, Germany) and ImageJ software[39] (National Institutes of Health, Bethesda, MD, USA). All images shown in the paper are representative of at least 3 independent experiments with a minimum of 15 images.

Confocal Airyscan microscopy

Fixed cells were imaged with a Zeiss LSM 880 Airyscan microscope (Carl Zeiss MicroImaging GmbH, Jena, Germany), equipped with an Ar-Laser Multiline (458/488/514nm), a DPSS-561 10 (561nm), a Laser diode 405-30 CW (405 nm), and a HeNe-laser (633nm). The objective used was a Zeiss plan-Apochromat 63xNA/1.4 oil DICII. The images were acquired with the Airyscan detector with a voxel size of 0.035 x 0.035 x 0.144µm for high resolution imaging and super-resolution processing resulting in a final resolution of 120 x 120 x 350 nm. Image acquisition, processing and analysis were performed with the ZEN 2.3 SP1 basic software (Carl Zeiss), or with ZEN 2.3 Blue (Carl Zeiss). 3D visualization of z-stacks was done using Imaris 7.7.2 (Bitplane AG, Zürich, Switzerland). Manders' and Pearson's colocalization measurements were done in ZEN 2.3 Blue with a Costes automatic thresholding. Bitplane Imaris software was used to generate surface renderings of 3D-SIM images. All images shown in the paper are representative of at least 3 independent experiments with a minimum of 15 images.

Live microscopy

Cells seeded into glass bottom imaging dishes were imaged on a DeltaVision microscope (Applied Precision) equipped with Elite TruLight Illumination System, a CoolSNAP HQ2 camera and a 40× or 60× Plan Apochromat (1.42 NA) lenses. For temperature control during live observation, the microscope stage was kept at 37 °C by a temperature-controlled incubation chamber. Time-lapse images deconvolved using the softWoRx software (Applied Precision, GE Healthcare) and processed with ImageJ for presentation and quantifications. Cells were imaged in DMEM gfp-2 anti-bleaching live-cell imaging medium (Evrogen) supplemented with 10% fetal bovine serum (FBS). Environmental control was provided by a heated stage and an objective heater (20-20 Technologies). SNAP-Cell® 647-SiR (SiR-SNAP 1:2000) (New England Biolabs) was used to detect SNAP-tagged alleles. SiR-DNA (1:2000) (SpiroChrome)[40] was used to monitor nuclei and micronuclei. Images were deconvolved using softWoRx software and processed in ImageJ/FIJI[39] or Imaris. Nuclear ruptures are identified by compromised nucleocytoplasmic compartmentalization as visualized by the equalization of 2xmRuby3-NES intensity between the (micro-)nucleus and cytoplasm. For quantification of nucleo-cytoplasmic compartmentalization in living cells (Fig.2a, Extended Data Fig.3c, 8c), regions of interest (ROIs) were drawn in the nucleus and cytoplasm, followed by extraction of the mean fluorescence intensity, background fluorescence subtraction, and calculation of [N]/[C] ratios. For cells with intact nuclei [N]/[C] ratio approximates 0.5, while for cells with ruptured nuclei this ratio approximates 1. All images and movies shown in the paper are representative of at least 3 independent experiments.

High-content microscopy

For quantification of LEMD2-CHMP7-CHMP4B positive micronuclei and TREX1 enrichment experiments Olympus ScanR system (illumination system with an UPLSAPO 40X objective) was used for imaging of a large number of cells in fixed samples and stained for the proteins of interest.

Correlative light and electron microscopy

Cells for CLEM experiments were grown on photo-etched coverslips (Electron Microscopy Sciences, Hatfield, USA). Fixation was done with 4% formaldehyde, 0.1%

glutaraldehyde in 0.1 M PHEM (240 mM PIPES, 100 mM HEPES, 8 mM $MgCl_2$, 40 mM EGTA), pH 6.9, for 1h. The coverslips were washed with 0.1 M PHEM buffer and mounted with Mowiol containing 1 µg/ml Hoechst 33342. The cells were examined with a Zeiss LSM710 confocal microscope (Carl Zeiss MicroImaging GmbH, Jena, Germany) equipped with a Laser diode 405-30 CW (405nm), an Ar-Laser Multiline (458, 488, 514 nm), a DPSS-561 10 (561 nm) and a HeNe-laser (633 nm). Cells of interest were identified by fluorescence microscopy and a Z-stack covering the whole cell volume was acquired. The relative positioning of the cells on the photo-etched coverslips was determined by taking a low magnification DIC image. The coverslips were removed from the object glass, washed with 0.1 M PHEM buffer and fixed in 2% glutaraldehyde/0.1 M PHEM overnight. Cells were postfixed in osmium tetroxide and potassium ferry cyanide, stained with tannic acid, and uranyl acetate and thereafter dehydrated stepwise to 100% ethanol followed by flat-embedding in Epon. Serial sections (80 nm - 200 nm) were cut on a Ultracut UCT ultramicrotome (Leica, Germany) and collected on formvar coated slot-grids. Thin sections were observed at 80 kV in a JEOL-JEM 1230 electron microscope and images were recorded using iTEM software with a Morada camera (Olympus, Germany). Sections of 200 nm thickness were observed at 200 kV in a Thermo ScientificTM TalosTM F200C microscope and recorded with a Ceta 16M camera. Consecutive sections were used to align electron micrographs with fluorescent images in X, Y and Z. For tomograms, image series of 200 nm thick section were taken between -60° and 60° tilt angles with 2° increment. Single-tilt axes series were recorded with a Ceta 16M camera. Tomograms were computed using weighted back projection using the IMOD package. Display, segmentation and animation of tomograms were also performed using IMOD software version 4.9[41].

Immunoblotting

Cells were lysed in 2x sample buffer (100 mM Tris-HCl pH 6.8, 4% SDS, 20% glycerol, 200 mM DTT, bromophenol blue). The whole-cell lysate was subjected to SDS-PAGE on a 4-20% gradient gel. Proteins were transferred to Immobilon-P membrane (Millipore). Immunodetection was performed using fluorescently-labeled secondary antibodies and Odyssey® or ChemiDoc™ developer. Western blot images are representatives for at least three independent experiments.

Real-Time quantitative PCR (RT-qPCR) analysis

Total RNAs were extracted using RNeasy® Mini Kit, ref. 74106, Qiagen, Germany. Reverse transcription was performed on 500 ng of DNAseI treated total RNA, with high-capacity cDNA reverse transcription kit, following manufacturer's recommendations (Applied Biosystems, ref. 4368814, USA). RT-qPCR was performed on 2 µl of 1/25 diluted cDNA with a CFX-96 (Biorad) thermocycler, using SsoAdvanced™ Universal SYBR Green Supermix 2X, Biorad. The following primers were used (Invitrogen) *CHMP7-FLAG* (Forward GTCACAGTCCTCGAGCAGAA / Reverse TACGTCGTTAACAGGGCTCA), *PPIA* (Forward ATGCTGGACCCAACACAAAT / Reverse TCTTTCACTTTGCCAAACACC) at a final concentration of 250 nM. All measurements were normalized to the expression of *PPIA*. Results were analysed using the $2^{-\Delta\Delta CT}$ method and are presented as the mean of three independent experiments.

Metaphase spreads

RPE1 cells stably expressing 2xmRuby-NES and DOX-inducible CHMP7-FLAG or CHMP7^{NES*}-FLAG were treated with 500 ng/ml DOX. After 4 hours, colchicine was added to the medium, the cells were incubated for another 20 hours, and harvested according to Mandahl (1992). Chromosomes of the dividing cells were then G-banded with Wright stain (Merck, Darmstad, Germany). The subsequent cytogenetic analysis and karyotypic description followed the recommendations of the International System for Human Cytogenetic Nomenclature (ISCN 2106).

In silico experiments

The geometry of the *in silico* experiments consists of a spherical cell and a smaller, concentric nucleus, populated by two types of particle, CHMP7 and LEMD2. LEMD2 is located on the INM and CHMP7 is either located in the cytoplasm or on the outer nuclear membrane (ONM)/ER. During the *in silico* experiments, the number of the LEMD2 sites bound with CHMP7 is monitored following simulated rupture of the nuclear envelope. The CHMP7-LEMD2 interaction is a reversible reaction with a forward rate of F_L and a backwards rate D_L. The values for all relevant variables are listed in Table 1.

For localization, two settings for CHMP7 are considered. In the first case, CHMP7 is treated as soluble and is free to diffuse in the cytoplasm in 3D. In the second case, CHMP7 is tethered to the ONM/ER and diffusion is restricted to 2D on the surface. Since the surface area of the ER is orders of magnitude larger than the nuclear membrane, we assume the CHMP7 particles on the ONM are in contact with a reservoir: when a particle moves from the outer to inner membrane, a new particle is placed randomly on the ONM in order to keep the concentration constant.

Three phenomena were modeled to capture the key behaviour of the system: diffusion, reactions and decay. In free (3D) diffusion, the particles are expected to perform random walks, as given by $\langle \delta x^2 \rangle = 6D\delta t$, where D is the diffusion constant of the particle. In our model we implement this by allowing each particle to jump a distance, j, in 3D space at each time-step with a probability, P_{walk}, given by

$$P_{\text{walk}} = 1 - \exp(-\Delta t/\tau) \,, \qquad (2)$$

where τ is the waiting time of the particle and Δt is the time-step of the simulation. The value of τ is chosen to ensure consistency between our simulation and the expected physical results:

$$\tau = \frac{j^2}{6D} \,. \qquad (3)$$

This particular implementation was chosen to simplify the calculation of reaction probabilities.

In the soluble (3D) CHMP7 scenario, if the jump would take the particle through a membrane barrier, the particle is bounced off the membrane instead, unless it would pass through the nuclear envelope rupture. Once a CHMP7 particle is bound to a LEMD2 particle it is immobilized until the complex decays.

In the case of membrane-bound CHMP7 (2D), diffusion is modeled on a spherical surface. The particles were created on the sphere by picking their location uniformly for $\theta \in [0,2\pi)$ and $\cos\phi \in [-1,1)$, since picking the positions uniformly in ϕ would result in an overrepresentation of particles at the poles[42]. To ensure that a particle moves in a uniform manner, a temporary particle P_0 was generated on the sphere a distance j away from the north pole at an angle $\psi \in [0,2\pi)$. The particle is then rotated twice about the origin of the sphere, using the same rotations that would carry the pole of the sphere on to the old position of the particle at (θ, ϕ). As distances are conserved during the rotation, the new particle is now a distance j away from its old position at a uniformly distributed angle, as we required. This means the resultant position P is given by;

$$P = P_0 R_Y(\phi) R_Z(\theta) \,, \qquad (4)$$

where R_Y and R_Z are the standard 3D rotation matrices.

Following a CHMP7 particle jump, the distance to the closest LEMD2 particle is measured. If this distance is within a collision distance, r_c, the probability for a CHMP7 particle to combine with a LEMD2 particle and act as a single complex until decay is given by

$$P_{CHMP7+LEMD2} = \frac{F_L}{4/3\pi r_C^3 N_A} \frac{1}{2-e^{-\Delta t/\tau_{CHMP}}-e^{-\Delta t/\tau_{LEMD}}} \quad (5),$$

where N_A is the Avogadro's constant.

The full derivation of this is given in [43]. From eq. 5, we are free to choose the value of r_c to fix $P_{CHMP7+LEMD2}$ (or the probity to fix the radius). Decreasing the collision radius increases the accuracy of the simulation, provided we do not allow $P > 1$. To prevent exceeding this limit, a constant value of r_c = 50 nm for both reactions is chosen.

As the reaction is bi-directional, separation of the complexes was also considered. Provided that the decay rate is much lower than the inverse of the simulation time step, $D_L \ll 1/\Delta t$, the probability of a CHMP7·LEMD2 complex dissociating into its separate component particles per time-step is defined as,

$$P_{\text{split,L}} = 1 - \exp(-D_L \Delta t)\,. \qquad (6)$$

Data visualization focused on the density of the LEMD2-bound CHMP7 particles and the location of these complexes.

Image processing

For measurement of LEMD2 intensity increase and changes in micronuclei circularity upon rupture (Fig. 3e, Fig. 4b), the perimeter of the micronuclei was manually drawn using LEMD2 signal as membrane proxy. The z-section corresponding to the middle plane of each micronuclei was chosen. For quantification of CHMP4B-eGFP and CHMP4B^{4DE}-eGFP intensity at micronuclei (Fig. 2b), micronuclei area was segmented by Otzu thresholding based on the DNA channel. The ImageJ f.unction “Analyze Particles” was then used to define ROIs and the mean intensity for the GFP channel of each ROI was measured. A band-shaped ROI around micronuclei was used to measure mean intensity of the cytoplasm as regularization factor. Image processing was performed using ImageJ/FIJI software[39]. For quantification of TOP2B accumulation (Fig. 4b), the area around nuclei was selected according to DNA staining and number of TOP2B foci was measured by using the “Count Maxima” function with tolerance values determined for each

experiment depending on the imaging parameters. For measurement of CHMP4B and RPA2 fluorescence intensity at micronuclei (Extended Data Fig. 10c), micronuclei area was segmented by Otzu thresholding based on the DNA channel. The ImageJ function "Analyze Particles" was then used to define ROIs and the mean intensity for the CHMP4B and the RPA2 channels of each ROI were measured. A band-shaped ROI around micronuclei was used to measure mean intensity of the cytoplasm in both channels as regularization factor. For quantification of DOX wash out experiments, cells were washed twice with 1x PBS after 16 hours of DOX incubation (500 ng/ml) and fresh DMEM-F12 complete media without DOX was added to the cells. The same protocol was used for confocal microscopy, western blot and RT-PCR. For quantification of the number CHMP4B foci at each time point, the area around nuclei was selected according to DNA staining, and the number of CHMP4B foci was measured for each cell using the Image J/FIJI "Count Maxima" function. Tolerance values were determined for each experiment, depending on the imaging parameters. Three independent experiments were performed. All data points were plotted using Graphpad Prism.

Data availability

The datasets generated and/or analyzed during the current study are available from the corresponding authors on reasonable requests.

Table 1.

Table 1. Variables used for *in silico* experiments.	
Parameter	**Value**
CHMP7+LEMD2 binding affinity	40 nM
Cell volume	2000 μm^3
Primary nucleus volume	400 μm^3
Micronucleus volume	4 μm^3

Rupture diameter	100 nm
CHMP7 density (Cytoplasmic)[44-48]	12 /μm³
CHMP7 density (ER-associated)[44-48]	2 /μm²
LEMD2 density[45-48]	100 /μm²
CHMP7 diffusion rate (Cytoplasmic)[49,50]	40 $\mu m^2/s$
CHMP7 diffusion rate (ER-associated)[51,52]	0.5 $\mu m^2/s$
LEMD2 diffusion rate[53,54]	0 $\mu m^2/s$
Bound LEMD2 limit	0.5
D_L	0.01 /s
F_L	4e-6 /M /s

1 Mierzwa, B. E. *et al.* Dynamic subunit turnover in ESCRT-III assemblies is regulated by Vps4 to mediate membrane remodelling during cytokinesis. *Nature cell biology* **19**, 787-798, doi:10.1038/ncb3559 (2017).

2 Schoneberg, J., Lee, I. H., Iwasa, J. H. & Hurley, J. H. Reverse-topology membrane scission by the ESCRT proteins. *Nat Rev Mol Cell Biol* **18**, 5-17, doi:10.1038/nrm.2016.121 (2017).

3 Christ, L., Raiborg, C., Wenzel, E. M., Campsteijn, C. & Stenmark, H. Cellular Functions and Molecular Mechanisms of the ESCRT Membrane-Scission Machinery. *Trends in biochemical sciences* **42**, 42-56, doi:10.1016/j.tibs.2016.08.016 (2017).

4 Vietri, M. *et al.* Spastin and ESCRT-III coordinate mitotic spindle disassembly and nuclear envelope sealing. *Nature* **522**, 231-235, doi:10.1038/nature14408 (2015).

5 Olmos, Y., Perdrix-Rosell, A. & Carlton, J. G. Membrane Binding by CHMP7 Coordinates ESCRT-III-Dependent Nuclear Envelope Reformation. *Current biology : CB* **26**, 2635-2641, doi:10.1016/j.cub.2016.07.039 (2016).

6 Gu, M. *et al.* LEM2 recruits CHMP7 for ESCRT-mediated nuclear envelope closure in fission yeast and human cells. *Proc Natl Acad Sci U S A* **114**, E2166-E2175, doi:10.1073/pnas.1613916114 (2017).

7 Arii, J. *et al.* ESCRT-III mediates budding across the inner nuclear membrane and regulates its integrity. *Nat Commun* **9**, 3379, doi:10.1038/s41467-018-05889-9 (2018).
8 Stuchell-Brereton, M. D. *et al.* ESCRT-III recognition by VPS4 ATPases. *Nature* **449**, 740-744, doi:10.1038/nature06172 (2007).
9 Fung, H. Y., Fu, S. C. & Chook, Y. M. Nuclear export receptor CRM1 recognizes diverse conformations in nuclear export signals. *Elife* **6**, doi:10.7554/eLife.23961 (2017).
10 Kirli, K. *et al.* A deep proteomics perspective on CRM1-mediated nuclear export and nucleocytoplasmic partitioning. *Elife* **4**, doi:10.7554/eLife.11466 (2015).
11 Webster, B. M. *et al.* Chm7 and Heh1 collaborate to link nuclear pore complex quality control with nuclear envelope sealing. *EMBO J* **35**, 2447-2467, doi:10.15252/embj.201694574 (2016).
12 Keppler, A., Pick, H., Arrivoli, C., Vogel, H. & Johnsson, K. Labeling of fusion proteins with synthetic fluorophores in live cells. *Proc Natl Acad Sci U S A* **101**, 9955-9959, doi:10.1073/pnas.0401923101 (2004).
13 Webster, B. M., Colombi, P., Jager, J. & Lusk, C. P. Surveillance of nuclear pore complex assembly by ESCRT-III/Vps4. *Cell* **159**, 388-401, doi:10.1016/j.cell.2014.09.012 (2014).
14 Hatch, E. M., Fischer, A. H., Deerinck, T. J. & Hetzer, M. W. Catastrophic nuclear envelope collapse in cancer cell micronuclei. *Cell* **154**, 47-60, doi:10.1016/j.cell.2013.06.007 (2013).
15 Denais, C. M. *et al.* Nuclear envelope rupture and repair during cancer cell migration. *Science* **352**, 353-358, doi:10.1126/science.aad7297 (2016).
16 De Vos, W. H. *et al.* Repetitive disruptions of the nuclear envelope invoke temporary loss of cellular compartmentalization in laminopathies. *Hum Mol Genet* **20**, 4175-4186, doi:10.1093/hmg/ddr344 (2011).
17 Olmos, Y., Hodgson, L., Mantell, J., Verkade, P. & Carlton, J. G. ESCRT-III controls nuclear envelope reformation. *Nature* **522**, 236-239, doi:10.1038/nature14503 (2015).
18 Raab, M. *et al.* ESCRT III repairs nuclear envelope ruptures during cell migration to limit DNA damage and cell death. *Science* **352**, 359-362, doi:10.1126/science.aad7611 (2016).
19 Zhang, C. Z. *et al.* Chromothripsis from DNA damage in micronuclei. *Nature* **522**, 179-184, doi:10.1038/nature14493 (2015).
20 Mackenzie, K. J. *et al.* cGAS surveillance of micronuclei links genome instability to innate immunity. *Nature* **548**, 461-465, doi:10.1038/nature23449 (2017).
21 Harding, S. M. *et al.* Mitotic progression following DNA damage enables pattern recognition within micronuclei. *Nature* **548**, 466-470, doi:10.1038/nature23470 (2017).
22 Bakhoum, S. F. *et al.* Chromosomal instability drives metastasis through a cytosolic DNA response. *Nature* **553**, 467-472, doi:10.1038/nature25432 (2018).
23 Liu, S. *et al.* Nuclear envelope assembly defects link mitotic errors to chromothripsis. *Nature* **561**, 551-555, doi:10.1038/s41586-018-0534-z (2018).
24 Crasta, K. *et al.* DNA breaks and chromosome pulverization from errors in mitosis. *Nature* **482**, 53-58, doi:10.1038/nature10802 (2012).
25 Willan, J. *et al.* ESCRT-III is necessary for the integrity of the nuclear envelope in micronuclei but is aberrant at ruptured micronuclear envelopes generating damage. *Oncogenesis* **8**, 29, doi:10.1038/s41389-019-0136-0 (2019).
26 Sagona, A. P., Nezis, I. P. & Stenmark, H. Association of CHMP4B and autophagy with micronuclei: implications for cataract formation. *Biomed Res Int* **2014**, 974393, doi:10.1155/2014/974393 (2014).
27 Robijns, J., Houthaeve, G., Braeckmans, K. & De Vos, W. H. Loss of Nuclear Envelope Integrity in Aging and Disease. *International review of cell and molecular biology* **336**, 205-222, doi:10.1016/bs.ircmb.2017.07.013 (2018).

28 Chen, R. & Wold, M. S. Replication protein A: single-stranded DNA's first responder: dynamic DNA-interactions allow replication protein A to direct single-strand DNA intermediates into different pathways for synthesis or repair. *Bioessays* **36**, 1156-1161, doi:10.1002/bies.201400107 (2014).
29 Brachner, A., Reipert, S., Foisner, R. & Gotzmann, J. LEM2 is a novel MAN1-related inner nuclear membrane protein associated with A-type lamins. *J Cell Sci* **118**, 5797-5810, doi:10.1242/jcs.02701 (2005).
30 De Vlaminck, I. *et al.* Torsional regulation of hRPA-induced unwinding of double-stranded DNA. *Nucleic Acids Res* **38**, 4133-4142, doi:10.1093/nar/gkq067 (2010).
31 Canela, A. *et al.* Genome Organization Drives Chromosome Fragility. *Cell* **170**, 507-521 e518, doi:10.1016/j.cell.2017.06.034 (2017).
32 Wolf, C. *et al.* RPA and Rad51 constitute a cell intrinsic mechanism to protect the cytosol from self DNA. *Nat Commun* **7**, 11752, doi:10.1038/ncomms11752 (2016).
33 Maciejowski, J., Li, Y., Bosco, N., Campbell, P. J. & de Lange, T. Chromothripsis and Kataegis Induced by Telomere Crisis. *Cell* **163**, 1641-1654, doi:10.1016/j.cell.2015.11.054 (2015).
34 Poser, I. *et al.* BAC TransgeneOmics: a high-throughput method for exploration of protein function in mammals. *Nat Methods* **5**, 409-415, doi:10.1038/nmeth.1199 (2008).
35 Campeau, E. *et al.* A versatile viral system for expression and depletion of proteins in mammalian cells. *PLoS One* **4**, e6529, doi:10.1371/journal.pone.0006529 (2009).
36 Dull, T. *et al.* A third-generation lentivirus vector with a conditional packaging system. *J Virol* **72**, 8463-8471 (1998).
37 Bache, K. G. *et al.* The ESCRT-III subunit hVps24 is required for degradation but not silencing of the epidermal growth factor receptor. *Mol Biol Cell* **17**, 2513-2523, doi:10.1091/mbc.e05-10-0915 (2006).
38 Sagona, A. P. *et al.* PtdIns(3)P controls cytokinesis through KIF13A-mediated recruitment of FYVE-CENT to the midbody. *Nat Cell Biol* **12**, 362-371, doi:10.1038/ncb2036 (2010).
39 Schindelin, J. *et al.* Fiji: an open-source platform for biological-image analysis. *Nat Methods* **9**, 676-682, doi:10.1038/nmeth.2019 (2012).
40 Lukinavicius, G. *et al.* SiR-Hoechst is a far-red DNA stain for live-cell nanoscopy. *Nat Commun* **6**, 8497, doi:10.1038/ncomms9497 (2015).
41 Kremer, J. R., Mastronarde, D. N. & McIntosh, J. R. Computer visualization of three-dimensional image data using IMOD. *J Struct Biol* **116**, 71-76, doi:10.1006/jsbi.1996.0013 (1996).
42 Marsaglia, G. Choosing a Point from the Surface of a Sphere. *The Annals of Mathematical Statistics* **43**, 2 (1972).
43 Ichikawa, K., Suzuki, T. & Murata, N. Stochastic simulation of biological reactions, and its applications for studying actin polymerization. *Phys Biol* **7**, 046010, doi:10.1088/1478-3975/7/4/046010 (2010).
44 Beck, M. *et al.* The quantitative proteome of a human cell line. *Mol Syst Biol* **7**, 549, doi:10.1038/msb.2011.82 (2011).
45 Geiger, T., Wehner, A., Schaab, C., Cox, J. & Mann, M. Comparative proteomic analysis of eleven common cell lines reveals ubiquitous but varying expression of most proteins. *Mol Cell Proteomics* **11**, M111 014050, doi:10.1074/mcp.M111.014050 (2012).
46 Nagaraj, N. *et al.* Deep proteome and transcriptome mapping of a human cancer cell line. *Mol Syst Biol* **7**, 548, doi:10.1038/msb.2011.81 (2011).
47 Wisniewski, J. R., Hein, M. Y., Cox, J. & Mann, M. A "proteomic ruler" for protein copy number and concentration estimation without spike-in standards. *Mol Cell Proteomics* **13**, 3497-3506, doi:10.1074/mcp.M113.037309 (2014).
48 Hein, M. Y. *et al.* A human interactome in three quantitative dimensions organized by stoichiometries and abundances. *Cell* **163**, 712-723, doi:10.1016/j.cell.2015.09.053 (2015).

49 Kuhn, T. *et al.* Protein diffusion in mammalian cell cytoplasm. *PLoS One* **6**, e22962, doi:10.1371/journal.pone.0022962 (2011).
50 Gura Sadovsky, R., Brielle, S., Kaganovich, D. & England, J. L. Measurement of Rapid Protein Diffusion in the Cytoplasm by Photo-Converted Intensity Profile Expansion. *Cell Rep* **18**, 2795-2806, doi:10.1016/j.celrep.2017.02.063 (2017).
51 Knight, J. D., Lerner, M. G., Marcano-Velazquez, J. G., Pastor, R. W. & Falke, J. J. Single molecule diffusion of membrane-bound proteins: window into lipid contacts and bilayer dynamics. *Biophys J* **99**, 2879-2887, doi:10.1016/j.bpj.2010.08.046 (2010).
52 Pawar, S., Ungricht, R., Tiefenboeck, P., Leroux, J. C. & Kutay, U. Efficient protein targeting to the inner nuclear membrane requires Atlastin-dependent maintenance of ER topology. *Elife* **6**, doi:10.7554/eLife.28202 (2017).
53 Carlson, B. E., Vigoreaux, J. O. & Maughan, D. W. Diffusion coefficients of endogenous cytosolic proteins from rabbit skinned muscle fibers. *Biophys J* **106**, 780-792, doi:10.1016/j.bpj.2013.12.044 (2014).
54 Ungricht, R., Klann, M., Horvath, P. & Kutay, U. Diffusion and retention are major determinants of protein targeting to the inner nuclear membrane. *J Cell Biol* **209**, 687-703, doi:10.1083/jcb.201409127 (2015).

Vietri et al. Fig. 1

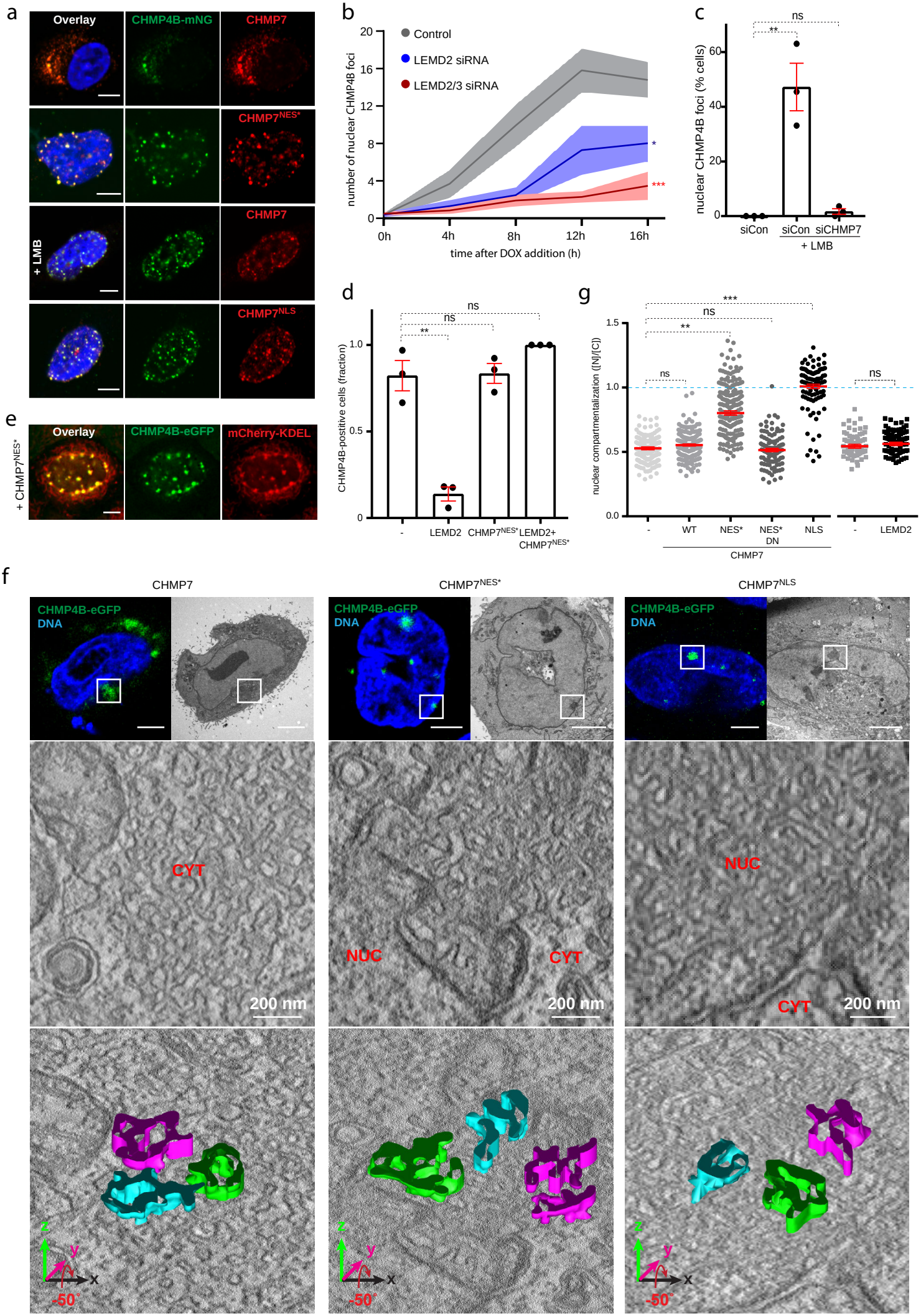

Vietri et al. Fig. 2

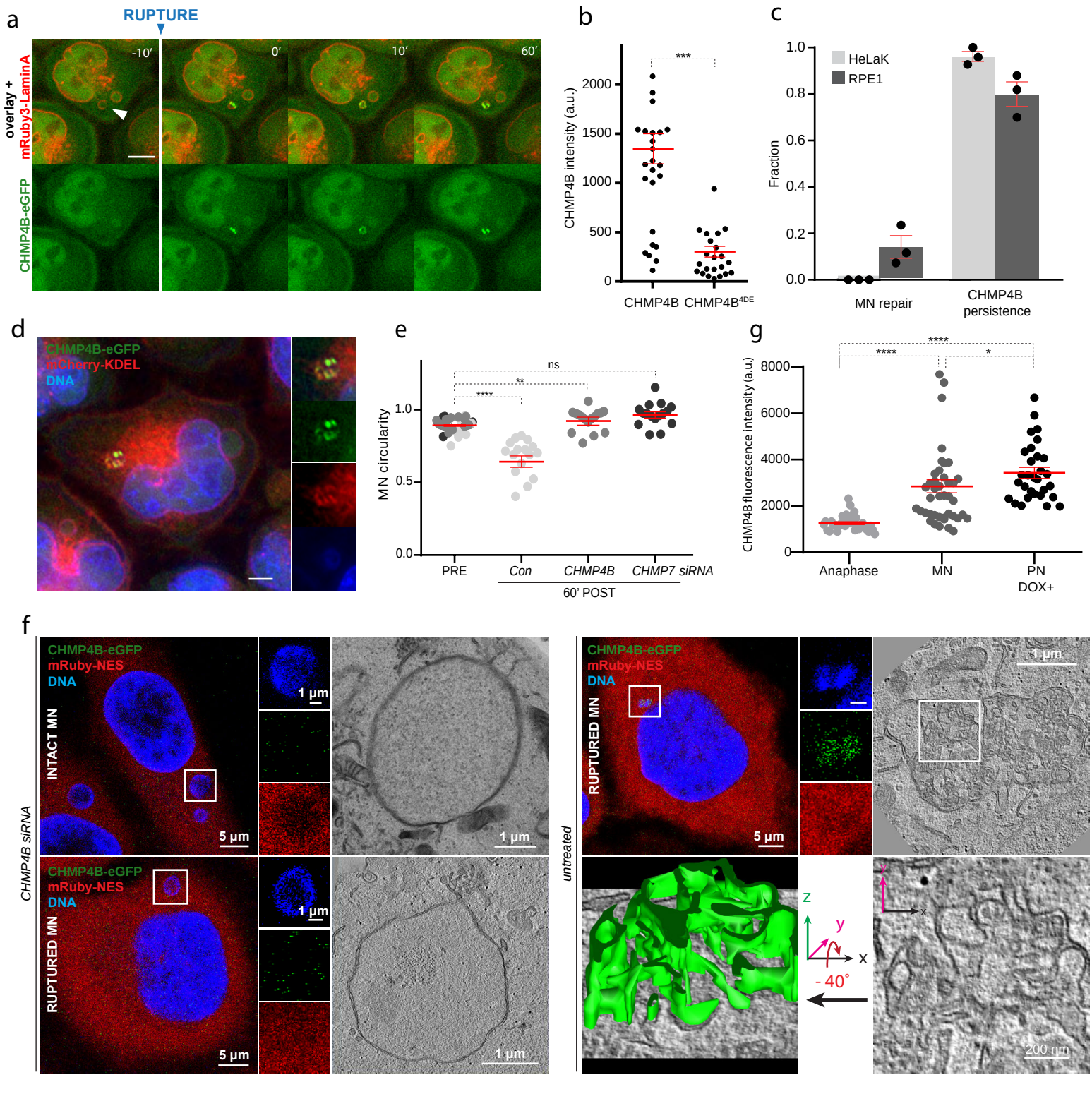

Vietri et al. Fig. 3

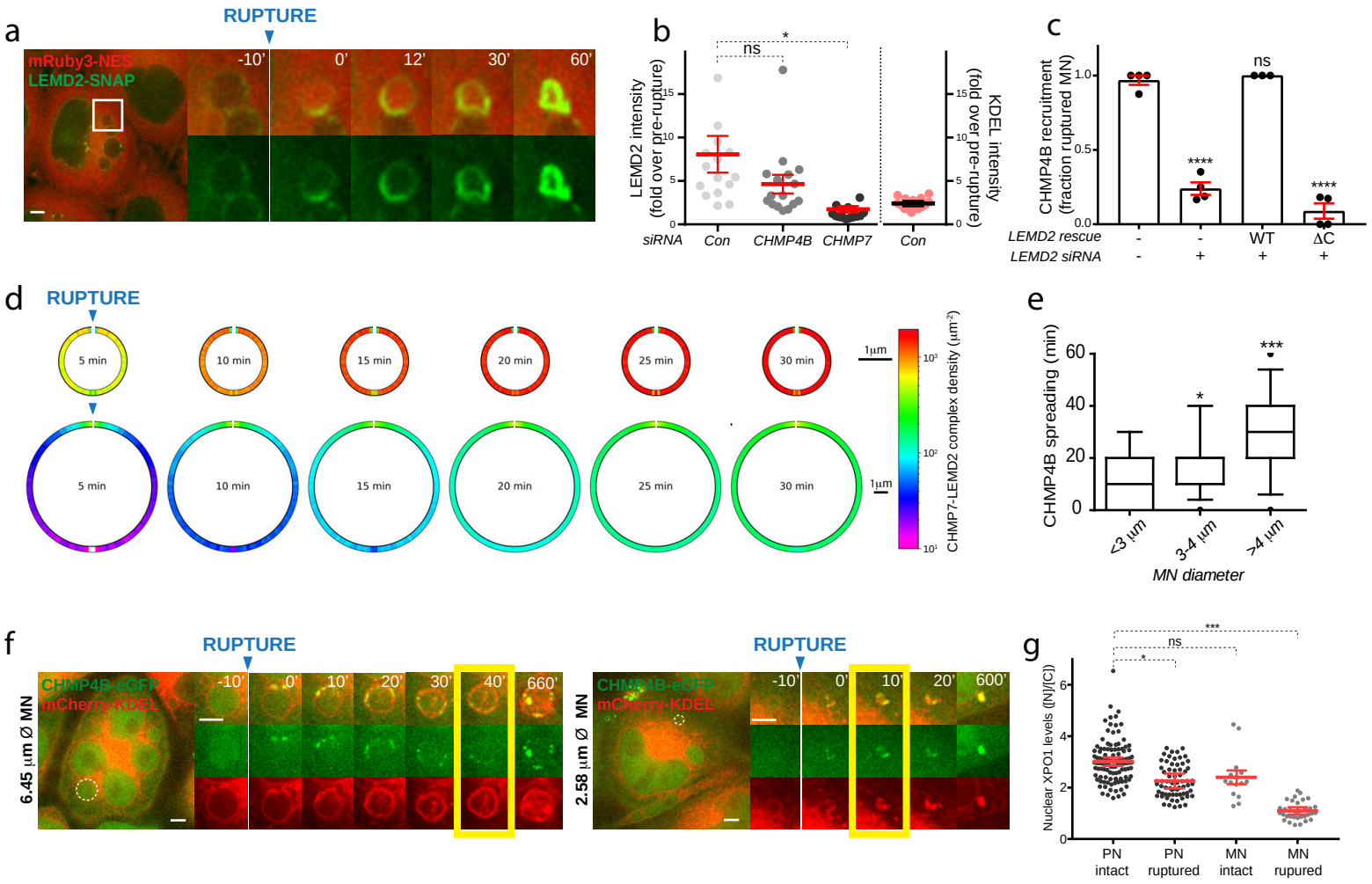

Vietri et al. Fig4